77 GHz FMCW Imaging Radar for Low Observable and Small Marine Target Detection in Dynamic Sea Conditions Based on Combined MIMO and DBS

Pirkani, Anum; Stove, Andrew; Kumar, Dillon; Cherniakov, Mike; Gashinova, Marina

DOI:
10.1109/TRS.2024.3400694

77 GHz FMCW Imaging Radar for Low Observable and Small Marine Target Detection in Dynamic Sea Conditions Based on Combined MIMO and DBS

Anum Pirkani, *Member, IEEE*, Andrew Stove, *Senior Member, IEEE,* Dillon Kumar*,* Mikhail Cherniakov, Marina Gashinova

***Abstract*— High resolution radar sensing is essential to provide situational awareness to small and medium sized marine platforms. However, detecting small targets on the sea surface is a challenging task for the marine surveillance radars because of the weak echoes and relatively low velocity. While there is a similarity and significant body of research on high resolution radar sensing in automotive environment, the direct translation of such techniques to marine sensing is difficult due to fundamentally dynamic underlaying sea surface. This paper addresses the need of developing novel radar sensing capabilities to image and, potentially, classify small marine targets, such as paddlers, buoys, flotsam and jetsam, or the incoming large waves. Our proposed approach combines Multiple Input, Multiple Output (MIMO) and Doppler Beam Sharpening (DBS) beamforming techniques with the Ordered Statistics – Cell Averaging Constant False Alarm Rate (OSCA-CFAR) for robust target detection, Density Based Spatial Clustering of Applications with Noise (DBSCAN) for clustering, and an adaptive focusing technique. With the developed methodology, multiple small 'dynamic' targets within the marine scene have been imaged and detected against substantially suppressed sea background.**

***Index Terms*— Clustering, DBSCAN, digital beamforming, Doppler beam sharpening, dynamic targets, high resolution sensing, mm-wave, 77 GHz radar, maritime sensing, MIMO, MIMO-DBS, beamforming, multiple-input multiple output, point spread function, OSCA-CFAR, target detection.**

I. Introduction

WITH the emergence of small agile sea vessels and increased use of recreational crafts, both manned and autonomous, there is a growing demand on new and robust sensing capabilities to provide a host platform with situational awareness, specifically, an ability to detect and avoid small 'uncatalogued' objects at the background of sea clutter. This will aid the navigation in open waters as well as in high density traffic and infrastructure scenarios of ports, channels etc.

Radar is a core sensing modality [1], providing an all-weather capability. The traditional marine radars, however, are hardly suitable for use on small boats being relatively large and cumbersome. Secondly, being designed to detect relatively large objects such as ships at long ranges, they cannot detect small targets, have a dead zone within minimum range due to eclipsed pulses, and have a low resolution [2]. This prevents them from seeing dangerous flotsam/jetsam, or other small objects, which can present a threat, such as sea drones able to carry a destroyer payload to even a large vessel, or, vice versa, be vulnerable to marine traffic, as in the case of sea creatures, swimmers, kayakers etc. Such objects may or may not possess additional Doppler shifts with respect to (w.r.t.) the sea surface, may be of small radar cross sections (RCS), and be non-cooperative (not sharing their location, position, and information about their class).

In addition to the requirement of detecting small objects, there is also a need to estimate the profile and direction of hazardous swells, so that the craft can plan their path and manoeuvre safely. Therefore, there are two conflicting requirements – the smaller is the vessel, the smaller are the objects which will present a potential danger to it, therefore high sensitivity and very high resolution, in particular angular resolution, are needed. However, this would require a larger physical antenna aperture, limiting its suitability for small platforms.

Several research efforts have been concerned with marine sensing intended for the detection and classification of small targets. These techniques often rely on the feature detection methods exploiting the differences between the characteristics of small sea-surface targets with that of sea surface such as using feature compression based detector [3], tri-feature based detector [4], dual tri-feature based detector [5], graph signal processing, where differences in the Doppler characteristics of target returns and sea clutter are exploited [6], non-linear time series analysis in fractal based detector, where different fractal characteristics of target returns and sea clutter are exploited [7], principal component analysis for anomaly detection in expected sea behaviour where sea clutter and target cells are classified in a feature space [8]. While these methods have shown a reasonable performance, they require a long observation time (in the order of second). This makes their

Manuscript submitted November 7, 2023.

This research was funded in whole by EPSRC UK grant EP/S033238/1 - 'Sub-THz Radar sensing of the Environment for future Autonomous Marine platforms – STREAM'. For the purpose of open access, a CC BY public copyright licence is applied to any AAM arising from this submission.

The authors express gratitude to the staff of Raymond Priestley Sport Centre of the University of Birmingham for support to organise and conduct trials from their site and use their boats and jetty for trials. We also thank our colleagues from The University of Saint Andrews for useful discussions. *(Corresponding author: A. Pirkani).*

The authors are affiliated with the School of Electronic, Electrical and Systems Engineering, University of Birmingham, Birmingham B15 2TT, U.K. (e-mail: a.a.a.pirkani@bham.ac.uk).

suitability for real-time path planning of a moving platform arguable. Furthermore, as they use limited feature set, they may have limited performance in characterising the differences between various marine targets and the complex sea conditions.

There is also an emergence of machine learning and neural networks based techniques [9], [10] where the networks are trained using the sea clutter data to predict the behaviour of sea clutter and identify the targets as potential anomalies. However, these approaches require vast and diverse datasets, collected in various sea conditions, which can be logistically impossible to collect. Moreover, the radar returns with targets are not used in the training process which might make their implementation questionable due to the diversity of small targets and their complicated interactions with the waves.

One of the key sensing technologies which has been significantly advanced in the recent years, especially in the automotive sensing sector, is the millimetre wave (mm-wave) radar, which is able to provide high resolution scene mapping [11] and has an ability to classify targets and clutter [12]. Indeed, to address the limitations imposed by the physical aperture constraints, techniques have been developed to enhance radar's resolution beyond the Rayleigh limit such as by forming a virtual aperture with the use of Multiple Input, Multiple Output (MIMO) principle [13]. Since MIMO operation does not involve scanning the antenna, it gives longer integration times and a wider field of view (FoV) as each transmit element transmits independently.

Though mm-wave radar would seem a good fit for the small marine vessels, for marine sensing it has been mostly researched in the context of understanding of propagation characteristics in the layer close to sea surface [14], [15]. The reason of limited research on mm-wave radar imaging in maritime environment is, probably, in the expected poor performance of small wavelength signals in the dynamic sea clutter and an associated non-linear target motion along the six degrees of freedom.

Imaging techniques using MIMO principle for marine sensing have been discussed in literature such as in [16], [17] where numerical simulations have been utilised to evaluate the performance of these radars to detect small marine vessels with slow-fluctuating RCS, and in [18] where a 24 GHz automotive MIMO radar has been used to detect and track small marine targets.

Inevitably, however, digital beamforming in MIMO radars leads to higher side lobe level (SLL) due to effective one-way antenna pattern formed by the multiplication of transmit and receive elements array factors. These sidelobes may significantly impede the dynamic range and target detection. Several techniques have been proposed to mitigate the issue of high side lobes and enhance the resolution beyond the MIMO virtual aperture, such as linearly constrained minimum variance and minimum variance distortionless response (MVDR) beamformers [19], multiple signal classification (MUSIC) [20], and array extrapolation [21]. These techniques, while effective, are computationally extensive and often require prior knowledge of the numbers of targets in the environment such as in the case of MVDR and MUSIC algorithms.

Synthetic aperture techniques exploiting the motion of host platform are other ways to refine angular resolution [22], [23]. One of such techniques is Doppler Beam Sharpening (DBS), currently being intensively developed for automotive applications [24], [25], [26], [27]. DBS takes advantage of the fine Doppler resolution and a wide differential Doppler shift of scatterers passing through the radar beam to provide high azimuth and cross-range resolutions while simultaneously lowering the SLL [26]. The performance of MIMO and DBS sensing modalities is complementary [27] as MIMO performs best for directions close to the boresight, and DBS performs best off-boresight due to increased Doppler spread of scatterers, which are supposed to remain stationary during the synthesis time.

However, in the case of marine sensor, additional efforts are required in order to focus the imagery of targets of interest as they might have finite displacement during integration time, caused by the movement of underlaying sea surface.

Thus, the detection of low-velocity small targets, such as buoys, small boats, icebergs, swimmers, small UAVs etc. remains a difficult problem due to their lower RCS, fluctuations in RCS, complex characteristics of sea clutter [28], and limited applicability of DBS in scenarios when both radar platform and target are moving, making it difficult to distinguish the Doppler shift caused by target's motion and that caused by radar's motion.

In this paper, the feasibility of MIMO-DBS beamforming at mm-wave frequencies is investigated for marine sensing for the first time in relation to the detection and imaging of multiple moving objects. We will (1) formulate a sensing strategy to decompose marine environment into the imagery of underlaying "stationary" background and moving targets with feature tracking, (2) develop adaptive MIMO-DBS beamforming approach to focus multiple dynamic targets, and (3) validate the approach by real-world experimentation.

The remainder of the paper is organised as follows: Section II gives the phenomenology of MIMO-DBS beamforming. The challenges in radar based maritime sensing are discussed in Section III. The signal processing approach for single and multi-target detection and focussing are discussed in Section IV. The measurement methodology and system configuration for the experimental validation of the approach developed with different platform dynamics and target characteristics are presented in Section V. Section VI analyses the results in various measurement scenarios and Section VII presents the conclusions and prospects.

II. Phenomenology of MIMO, DBS, and MIMO-DBS Beamforming

In this section we will briefly outline the background theory to define notation and terminology for the integrity of the material presented in the paper.

DBS utilises the difference in relative Doppler frequency shift of scatterers at different angles with respect to the moving radar platform to estimate the spatial position of target. Based on the Doppler spread of scatterers across the radar beam, the physical beam is divided into finer sub-beams, as illustrated in Fig. 1. The scatterers located within different

sub-beams are resolved after Doppler processing to accurately represent the extent of the target.

In this work, coherent frequency modulated continuous wave (FMCW) signal is used with the transmitted waveform expressed as:

$$S_{\mathrm{Tx}}(t) = A_{\mathrm{T}} \exp\left(j\left(\omega_{\mathrm{c}} t + \pi K t^2\right) + \phi\right) \tag{1}$$

where A_{T} is the amplitude of transmitted signal, $\omega_{\mathrm{c}} = 2\pi f_{\mathrm{c}}$ is the angular frequency for carrier frequency f_{c}, K is the sweep rate, and ϕ is the initial phase. As the radar is coherent, initial phase will be preserved and hereafter not included in the mathematical expressions.

The signal received by the radar installed on a platform moving with speed v_{p} is expressed as:

$$S_{\mathrm{Rx}}(t) = A_{\mathrm{R}} \exp\left(j\left(\omega_{\mathrm{c}}\left(t-\tau_{\mathrm{D}}\right) + \pi K\left(t-\tau_{\mathrm{D}}\right)^2\right)\right) \tag{2}$$

where A_{R} is the amplitude of received signal. Its value depends upon the propagation environment between the radar and target and the target RCS, $\tau_{\mathrm{D}} = 2\left(R \pm v_{\mathrm{r}} t\right)/c$ is the two-way propagation delay between transmitted and received signals, R is the distance between the radar and target, $v_{\mathrm{r}} = v_{\mathrm{p}} \cos\theta_{\mathrm{T}}$ is the relative radial velocity of a target, and θ_{T} is the direction to the target w.r.t. radar boresight. The second term in the exponential represents frequency modulation, hereafter expressed as $\mu\left(t-\tau_{\mathrm{D}}\right)$. Therefore, the received signal can be expressed as:

$$S_{\mathrm{Rx}}(t) = A_{\mathrm{R}} \mu\left(t-\tau_{\mathrm{D}}\right) \mathrm{e}^{j\left(\omega_{\mathrm{c}} t - \omega_{\mathrm{c}} 2R/c \mp k 2 v_{\mathrm{p}} \cos\theta_{\mathrm{T}} t\right)} \tag{3}$$

where $k = 2\pi f_{\mathrm{c}}/c$ is the wave number.

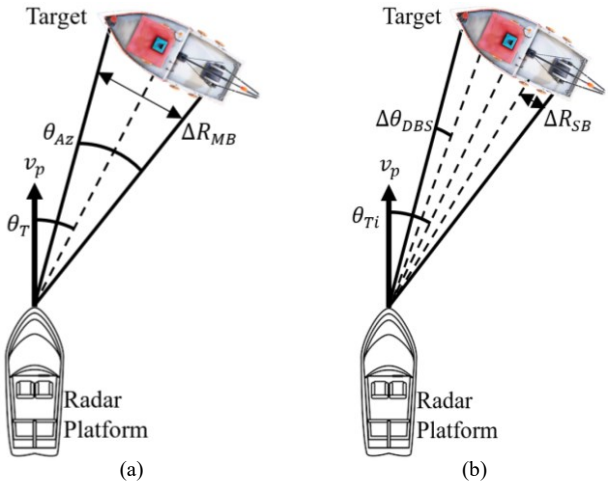

Fig. 1. Doppler beam sharpening concept illustration: (a) main beam of the physical aperture. v_p represents the platform velocity, θ_T represents the angle to the target, and θ_{Az} and ΔR_{MB} represents the azimuth beamwidth and cross-range resolution of the physical aperture, respectively. (b) sub-beams formed by utilising the Doppler frequency difference of scatterers across the main beam. θ_{Ti} represents the angle of scatterer at sub-beam 'i,' and $\Delta\theta_{DBS}$ and ΔR_{SB} represents the 3-dB beamwidth and cross-range resolution after DBS processing.

To resolve scattering points representing a target along the Doppler or velocity dimension, sequential chirps will be integrated within a coherent processing interval (CPI). The received signal corresponding to chirp 'n' can be expressed as:

$$S_{\mathrm{Rx}}(t,n) = A_{\mathrm{R}} \mu\left(t-\tau_{\mathrm{D}}\right) e^{j\left(\omega_{\mathrm{c}} t - \omega_{\mathrm{c}} 2R/c \mp k 2 v_{\mathrm{p}} \cos\theta_{\mathrm{T}} CRI (n-1)\right)} \tag{4}$$

where *CRI* represents the chirp repetition interval.

In MIMO radar, angular refinement is achieved through the use of multiple transmit and receive elements while maintaining a small physical aperture size. The orthogonality of transmit signals allows formation of a virtual array of $N_{\mathrm{MIMO}} = N_{\mathrm{Tx}} N_{\mathrm{Rx}}$ elements, where N_{Tx} and N_{Rx} represents the number of transmit and receive elements, respectively. The received signal at m-th virtual array element is expressed as:

$$S_{\mathrm{Rx}}(t,n,m) = S_{\mathrm{Rx}}(t,n) e^{-jkd(m-1)\sin\theta_T} \tag{5}$$

where $d = \lambda/2$ is the spacing between virtual elements, λ is the wavelength, and the phase shift of received signal across consecutive array elements is expressed as $kd\sin\theta_{\mathrm{T}}$. $S_{\mathrm{Rx}}(t,n,m)$ denotes the 3-dimensional radar data with each dimensions representing the fast-time, slow-time, and array elements, respectively.

Based on (4) and (5), two steering vectors can be defined:

1) Steering vector of Doppler frequency, denoted as SV_{CPI}, representing the phase shift across N_{CPI} chirps within a CPI, expressed as:

$$SV_{\mathrm{CPI}}(\theta_{\mathrm{T}}) = \left[1 \; e^{-jk2v_{\mathrm{p}}CRI\cos\theta_{\mathrm{T}}} \ldots e^{-jk(N_{\mathrm{CPI}}-1)2v_{\mathrm{p}}CRI\cos\theta_{\mathrm{T}}}\right]^{\mathrm{T}} \tag{6}$$

2) Steering vector of MIMO array configuration, denoted as SV_{MIMO}, representing the phase shift across $N_{\mathrm{Tx}}N_{\mathrm{Rx}}$ array elements, expressed as:

$$SV_{\mathrm{MIMO}}(\theta_{\mathrm{T}}) = \left[1 \; e^{-jkd\sin\theta_{\mathrm{T}}} \ldots e^{-jkd(N_{\mathrm{Tx}}N_{\mathrm{Rx}}-1)\sin\theta_{\mathrm{T}}}\right]^{\mathrm{T}} \tag{7}$$

These steering vectors provide two independent means to estimate the direction to target, denoted as θ_{T}, where SV_{MIMO} is used for spatial compression in MIMO beamforming and SV_{CPI} is used for Doppler compression as the first step in DBS beamforming.

A. MIMO Beamforming

Using (7), the spatial frequency difference between scatterers located at θ_{T} and $\theta_{\mathrm{T}} + \Delta\theta_{\mathrm{MIMO}}$ where $\Delta\theta_{\mathrm{MIMO}}$ is the 3-dB resolution of virtual array is defined as:

$$\begin{aligned} \Delta\omega &= kd_{\mathrm{MIMO}}\left(\sin\left(\theta_{\mathrm{T}} + \Delta\theta_{\mathrm{MIMO}}\right) - \sin\theta_{\mathrm{T}}\right) \\ \Delta\omega &= kd_{\mathrm{MIMO}} \cos\theta_{\mathrm{T}} \cdot \Delta\theta_{\mathrm{MIMO}} \end{aligned} \tag{8}$$

where $d_{\mathrm{MIMO}} = N_{\mathrm{MIMO}}\lambda/2$ is the aperture size of MIMO array. The array factor is expressed as [27]:

$$\mathrm{AF}_{\mathrm{MIMO}} = \mathrm{sinc}\left(\frac{d_{\mathrm{MIMO}}}{\lambda}\cos\theta_{\mathrm{T}}\Delta\theta_{\mathrm{MIMO}}\right) \tag{9}$$

To estimate the 3-dB beamwidth, sinc square function obtained from (9) is equated to 0.5 and solved with the Taylor series expansion, resulting in:

$$\Delta\theta_{\mathrm{MIMO}} \approx \frac{1.22 \cdot \lambda \cdot \zeta_{\mathrm{w}}}{d_{\mathrm{MIMO}} \cos\theta_{\mathrm{T}}} \tag{10}$$

Here, we include a factor ζ_W to represent resolution coarsening due to applied spectral window before Fast Fourier transform (FFT) to suppress angular sidelobes.

As shown in (10), MIMO beamformer provides fine resolution close to the boresight and the resolution degrades with off-boresight angles.

B. DBS Beamforming

The sub-beams, illustrated in Fig. 1 (b), are synthesised within a CPI over which range-Doppler processing is performed. The directional angle of scatterer in each sub-beam is estimated as:

$$\theta_{Ti} = \arccos\left(\frac{\lambda f_{Di}}{2v_p}\right), \quad i = 1:N \tag{11}$$

where f_{Di} represents the Doppler frequency within sub-beam 'i' and N denotes the number of sub-beams.

Using (6), the spatial frequency difference between two scatterers located at θ_T and $\theta_T + \Delta\theta_{DBS}$ where $\Delta\theta_{DBS}$ is the Doppler resolution is defined as:

$$\begin{aligned} \Delta\omega &= 2kv_pT_F\left(\cos\left(\theta_T + \Delta\theta_{DBS}\right) - \cos\theta_T\right) \\ \Delta\omega &= 2kv_pT_F \sin\theta_T \Delta\theta_{DBS} \end{aligned} \tag{12}$$

where $T_F = N_{CPI} \cdot CRI$ represents the frame interval for Doppler processing. In Time Division Multiplexing (TDM) MIMO radar, equivalent CRI, hereafter expressed as MIMO frame repetition interval (MFRI), is $MFRI = CRI \cdot N_{Tx}$. MFRI represents the period from the beginning of one TDM-MIMO frame to the next. This gives $T_F = N_D \cdot MFRI$ and $N_D = N_{CPI}/N_{Tx}$ represents the number of chirps over which Doppler processing is performed.

Similar to the array factor in MIMO configuration, the array factor after DBS beamforming will also follow a sinc function that can be simplified to estimate the 3-dB beamwidth as:

$$\begin{aligned} \mathrm{AF}_{DBS} &= \mathrm{sinc}\left(\frac{2}{\lambda}T_F v_p \sin\theta_T \Delta\theta_{DBS}\right) \\ \Delta\theta_{DBS} &\approx \frac{1.22 \cdot \lambda \cdot \zeta_W}{2T_F v_p \sin\theta_T} \end{aligned} \tag{13}$$

Therefore, the resolution after DBS beamforming primarily depends on the platform velocity and frame interval over which Doppler processing is performed. The higher the values of these parameters are, the finer is the resolution due to expected wider Doppler spread from the scatterers. This however comes with challenges which will be discussed in Section III.

A comparison of (10) and (13) shows opposite trends of azimuth refinement with the off-boresight angles in MIMO and DBS processing, respectively.

C. MIMO-DBS Beamforming

Thus, to achieve a high-resolution wide scene imagery in both forward-looking and off-boresight directions, and to resolve the angular ambiguity on either side of the platform velocity vector, inherent for DBS, combined MIMO-DBS beamforming is applied by sampling the independent DBS and MIMO processed data at points where MIMO and DBS angles are equal. Due to different sampling densities in the azimuth and Doppler domains, we use spline interpolation to give common angular sampling.

From the array factors in (9) and (13), the 3-dB roll-off points after MIMO-DBS processing are estimated from the following expression.

$$\mathrm{sinc}^2\left(\frac{d_{MIMO}}{\lambda}\cos\theta_T \Delta\theta_{MIMO\text{-}DBS}\right) \cdot \mathrm{sinc}^2\left(\frac{2}{\lambda}T_F v_p \sin\theta_T \Delta\theta_{MIMO\text{-}DBS}\right) = \frac{1}{2} \tag{14}$$

where $\Delta\theta_{MIMO\text{-}DBS}$ is the angular sub-beam resolution after MIMO-DBS processing. Solving (14) with the Taylor series expansion gives:

$$\Delta\theta_{MIMO\text{-}DBS} \approx \frac{1.22 \cdot \zeta_W}{\sqrt{\left(\frac{d_{MIMO}}{\lambda}\cos\theta_T\right)^2 + \left(\frac{v_p}{\Delta v}\sin\theta_T\right)^2}} \tag{15}$$

where $\Delta v = \lambda/2T_F$ is the velocity resolution.

Fig. 2 shows the 3-dB resolutions of each beamformer: MIMO, DBS, and MIMO-DBS, with the latter two shown for two platform speeds of 5 m/s and 10 m/s. The plots are theoretically estimated for the configuration of INRAS Radarlog sensor [29] which has been used in the measurements, fully described in Section V. The radar configuration parameters and expected performance are presented in Table I.

TABLE I
CONFIGURATION PARAMETERS FOR INRAS RADARLOG.

Parameter	Value	Unit
Sweep Time	204.8	µs
Chirp repetition interval	230	µs
Mode of operation	TDM-MIMO	
MIMO frame repetition interval	1	ms
Sweep Bandwidth	2	GHz
Start Frequency	76	GHz
Effective Isotropic Radiated Power	27	dBm
Antenna Configuration (Tx, Rx)	4, 16	elements
Beamwidth (azimuth, elevation)	2.1, 16	degree
Noise Figure	13	dB
Range resolution	7.5	cm
Unambiguous range	76.8	m
Unambiguous velocity	±0.95	ms^{-1}
Doppler resolution	7.8	Hz
Velocity resolution	0.015	ms^{-1}
Integration Duration (CPI)	128	ms
Update rate	4.8	kHz

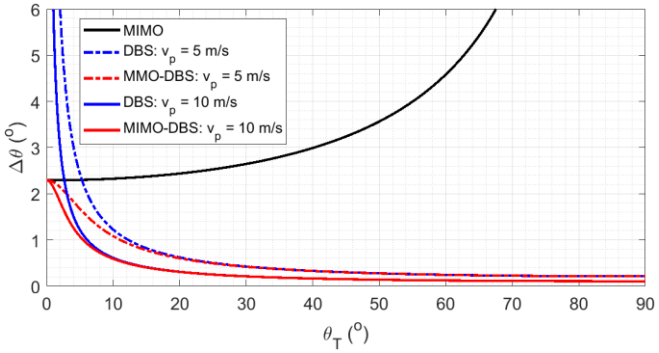

Fig. 2. Comparison of the resolution of MIMO, DBS, and MIMO-DBS beamformers.

The resolution refinement factor after MIMO-DBS processing, denoted as $\zeta_{\text{MIMO-DBS}}$, is estimated as the ratio of (15) and (10), and expressed as:

$$\zeta_{\text{MIMO-DBS}} = \frac{\lambda\sqrt{\left(\frac{d_{\text{MIMO}}}{\lambda}\cos\theta_{\text{T}}\right)^2+\left(\frac{v_{\text{p}}}{\Delta v}\sin\theta_{\text{T}}\right)^2}}{d_{\text{MIMO}}\cos\theta_{\text{T}}} \tag{16}$$

$\zeta_{\text{MIMO-DBS}}$ is plotted in Fig. 3 as a function of the direction to the target w.r.t. radar boresight, denoted as θ_{T}, for 3 platform speeds of 2 m/s, 5 m/s and 10 m/s. The point spread functions of each beamformer are estimated from their array patterns, and the respective range cuts are shown in Fig. 4 for a point target positioned at 5° and 20°. As expected, $\zeta_{\text{MIMO-DBS}}$ improves as the angle to the target increases.

From the aforementioned discussion, we should emphasise three important aspects of the MIMO-DBS technique:

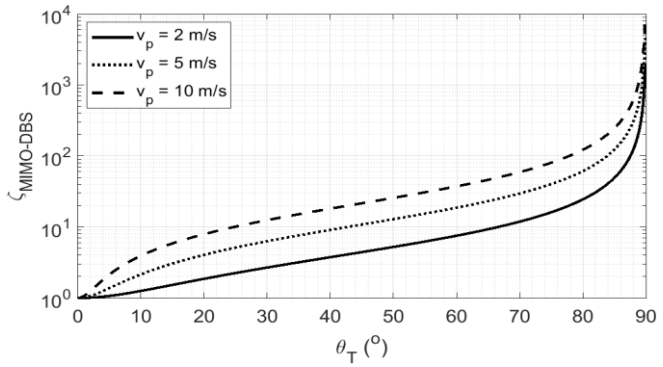

Fig. 3. Resolution refinement factor, denoted as $\zeta_{\text{MIMO-DBS}}$, after MIMO-DBS processing.

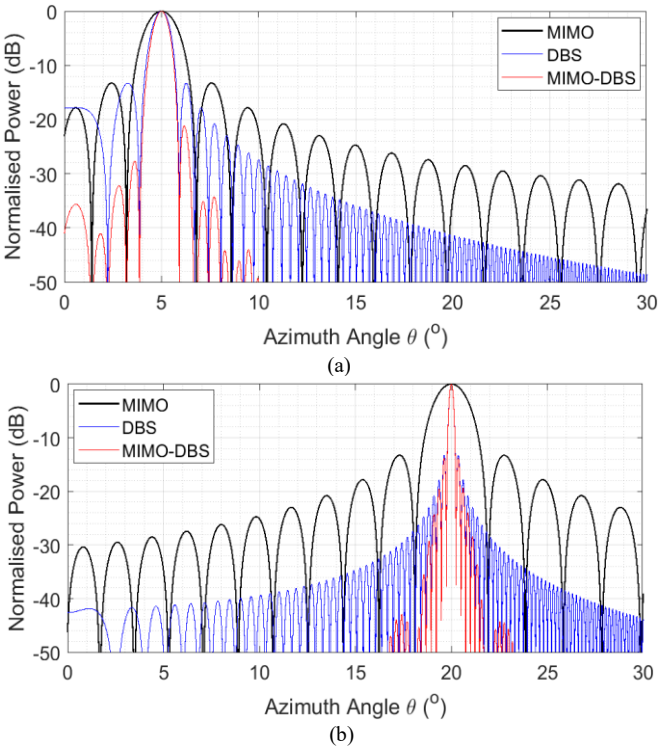

Fig. 4. Range cuts of the point spread functions after MIMO, DBS, and MIMO-DBS beamforming; (a) 5°, (b) 20°.

1) With combined MIMO-DBS beamforming, resolution refinement in obtained that depends upon the platform speed and the direction to the target.
2) While there is minimal improvement of the angular resolution at forward-looking direction, DBS still allows to reduce the side lobes significantly, and
3) With DBS angular refinement, the sub-beams are not evenly distributed over the main antenna beamwidth due to cosine relationship between the azimuth angle and Doppler shift.

This results in unequal cell sizes of the radar map, and for image processing, re-meshing is required [27].

D. Velocity Ambiguity and DBS Field of View

One of the major impediments in MIMO radars is the limited unambiguous velocity due to an increase in the equivalent MFRI, which is calculated as:

$$v_{\max} = \frac{\lambda}{4\cdot MFRI} \tag{17}$$

This leads to the issue of velocity aliasing, which if not accounted for leads to an incorrect mapping of the velocity to DBS angle as shown in (11).

To mitigate the ambiguities associated with signal aliasing, we precisely re-define the velocity vector within the range: $v_p - 2v_{\max} < v_{\text{bin}} \le v_p$. The velocity bins are then transformed according to the following:

$$v_{\text{bin}} = \begin{cases} v_p & \text{if } i_{\text{bin}} = \eta \\ v_p - (\eta - i_{\text{bin}})\,v_{res} & \text{if } i_{\text{bin}} < \eta \\ (v_p - 2v_{\max}) + (i_{\text{bin}} - \eta)\,v_{res} & \text{if } i_{\text{bin}} > \eta \end{cases} \tag{18}$$

where, $i_{\text{bin}} = 1, ..., N_D$ is the bin index and $\eta = v_{\text{p}}/\Delta v$. The radar data is then rearranged according to (18) across the slow-time dimension allowing us to accurately map the velocity to DBS angle.

Due to the rearrangement of velocity vector in (18), the effective FoV after DBS processing is limited to:

$$\theta_{\text{FoV-DBS}} = \begin{cases} \theta_{\text{FoV-MIMO}} & \text{if } v_{\text{p}} \le v_{\max} \\ \cos^{-1}\left(1 - \frac{2v_{\max}}{v_{\text{p}}}\right) & \text{otherwise} \end{cases} \tag{19}$$

where, $\theta_{\text{FoV-MIMO}}$ is the FoV after MIMO processing defined by the antenna element pattern and $\theta_{\text{FoV-DBS}}$ represents the FoV after DBS processing. To mitigate this effect, we replicate the radar datacube along the Doppler dimension after applying (18) to expand the FoV, as discussed in [30].

E. Platform Kinematics

DBS requires a knowledge of platform kinematics, including velocity, acceleration, and rotation expressed as a roll (rotation along direction of motion), pitch (rotation perpendicular to direction of motion), and yaw (rotation along vertical axis). In this work, these parameters are estimated using an inertial measurement unit (IMU). The methodology to obtain platform speed from these parameters, which will be later used in the measurement section, is discussed here. The illustration of a marine platform with platform kinematics is shown in Fig. 5.

Firstly, the rotations including roll, pitch, and yaw are used to define the Euler angles. From these angles, a rotation matrix

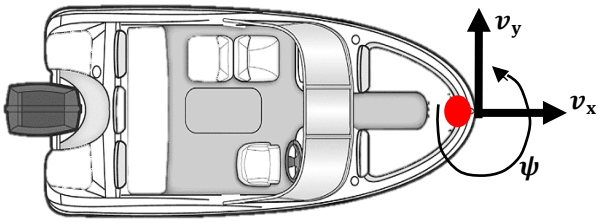

Fig. 5. Platform kinematics required for DBS. Red dot represents the sensor installation point and v_z is in the outward looking direction.

is generated, denoted as $\mathbf{R}_i$. This provides the direction of travel at each time instant. For example, if the direction of travel at $t = 0$ is $\mathbf{d}_o$, then directional vector at each consecutive time stamps is $\mathbf{d}_i = \mathbf{R}_i \|\mathbf{d}_{i-1}\|_2$ where $\|.\|_2$ is an operator representing the second norm. The speed at each time instant is then estimated as in [31]:

$$\mathbf{v}_i = \mathbf{v}_{i-1} + t_i \mathbf{A}_i + \mathbf{R}_i \|\mathbf{d}_{i-1}\|_2 \boldsymbol{\psi}_i = \mathbf{v}_{i-1} + \mathbf{A}_i t_i + \mathbf{d}_i \boldsymbol{\psi}_i \quad (20)$$

where t_i is the time difference between two time stamps, $\mathbf{v}_i$, $\boldsymbol{\psi}_i$, $\mathbf{A}_i$ are the velocity, angular velocity, and acceleration vectors along x, y, and z directions, respectively. The first two terms in (20) account for the velocity change due to translational motion of platform and the last term accounts for the effect of rotation on platform velocity. The norm value of $\mathbf{v}_i$ is used for DBS processing.

III. Challenges in Maritime Sensing

One of the major limitations on radar sensing in maritime conditions is imposed by the dynamic sea surface (due to the longitudinal and transversal motion of wave particles [32], [33]), making clutter returns from the water surface to be essentially non-stationary. The backscatter from surface have similar behaviour as the echoes from real targets [34], which can often mask the targets with relatively small RCS. The non-stationary marine environment impedes the performance of radar sensing, which is discussed in this section.

A. Effect of Wave Motion on Target

While the actual motion of water particles is complex and depends on many parameters, such as depth, pressure, wind etc., their general behaviour as the wave propagate in a medium, can be presented as a clockwise circular motion [32], illustrated in Fig. 6.

Based on this motion, two primary modes of mechanical wave can be defined, which are: (1) longitudinal mode, where particles displace along the direction of wave propagation, and (2) transversal mode, where particles oscillate up and down, perpendicular to the direction of propagation. The amount of vertical displacement depends upon the wave amplitude, whereas horizontal displacement depends upon the wavelength. For example, near the shore, due to smaller wavelength [35], horizontal displacement is smaller compared to a fully developed sea where larger wavelength causes a larger horizontal displacement.

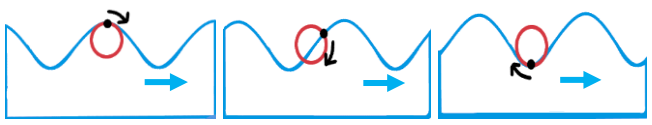

Fig. 6. Wave motion and target displacement.

Consequently, targets on the surface of water, particularly small targets, would sway with the wave in a similar manner, potentially moving through several resolution cells during the integration time of the radar. This might result in their non-zero Doppler frequency shift w.r.t. the radar.

B. Sea Surface Modelling and Characteristics

To estimate the expected displacement and velocity of a point target due to wave motion, we use sea surface modelling considering the amplitude and phase characteristics of the wave spectrum. The two distinct parts of a full directional spectrum are as follows [36]:

1) Empirical point (uni-directional) energy spectra, denoted as $s_{PM}(f)$, which we model for a fully developed sea based on the Pierson-Moskowitz formulations [37], calculated as:

$$s_{PM}(f) = \frac{\alpha g^2}{(2\pi)^4 f^5} e^{-\frac{5}{4}\left(\frac{f_m}{f}\right)^4}$$
$$f_m = \frac{g}{2\pi U_{19.5}} \sqrt[4]{\frac{4}{5}\beta} \quad (21)$$

where, f and f_m represents the frequency and modal frequency, respectively, g is the gravitational constant, and $U_{19.5}$ is the wind speed at 19.5 m above the sea surface. For example, to model a sea state of 1 (according to Douglas scale [38]), $\alpha = 0.0081$, $\beta = 0.74$, and $U_{19.5} = 2.8$ m/s [38].

2) Energy spreading function, denoted as $D(\vartheta, f)$, defines the angular distribution of waves, which we model based on the Longuet-Higgins spreading formulation [39], estimated as:

$$D(\vartheta, f) = \frac{2^{s-1} \cdot \Gamma(s+1)^2}{\pi \cdot \Gamma(s+1)} \left|\cos\frac{1}{2}\vartheta\right|^{2s}$$
$$s = \begin{cases} s_m (f/f_m)^5 & f \le f_m \\ s_m (f/f_m)^{-2.5} & f > f_m \end{cases} \quad (22)$$
$$s_m = 11.5(2\pi f_m U_{10}/g)^{-2.5}$$

where ϑ represents the spreading angle and U_{10} is the wind speed at 10 m above the sea surface which is considered as 2.6 m/s for a sea state 1 [38].

Under certain atmospheric conditions, the relationship between $U_{19.5}$ and U_{10} can be expressed as $U_{19.5} = 1.076 U_{10}$ [40].

The modelled surfaces for a sea state 1 and 5 are shown in Fig. 7 (a) and (b), respectively, and the displacements and velocities of a target positioned at 20 m from the radar during 1 s time span are presented in Fig. 7 (c) and (d), respectively for sea states 1 – 5.

The expected velocity of target for all the sea states is greater than the velocity resolution according to the parameters stated in Table I. This indicates that the target might traverse across several Doppler (velocity) bins during

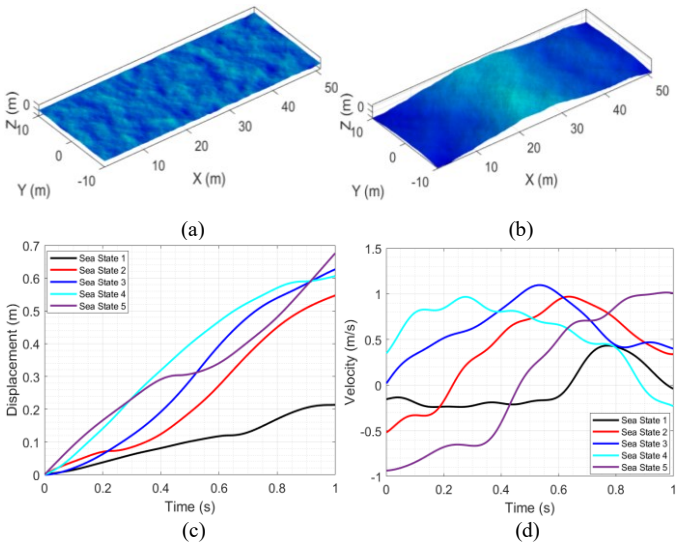

Fig. 7. Modelled sea surface and target motion: (a) sea surface for a sea state 1, (b) sea surface for a sea state 5, (c) expected displacement of target, (d) expected velocity of target.

signal processing. The expression of radial velocity can therefore be modified as following:

$$\mathbf{v}_{\mathrm{r}} = \left(\mathbf{v}_{\mathrm{p}} \pm v_{\mathrm{t}} \pm \gamma\right)\cos\theta_{\mathrm{T}} \tag{23}$$

where v_{t} represents the target motion and γ accounts for the platform and target motion due to wave dynamics. Both v_{t} and γ are unknown at the platform end, therefore, to account for such a complex motion, an adaptive process of mutual speed estimation will be used and presented in Section IV.

At higher sea states, the expected displacement and velocity will also increase. Nevertheless, these considerations are valid for the points of sea surface displacement, as well as for floating targets to some degree. Depending on the target weight and shape, it might have different motion parameters. When considering an integration of returns from a target using moving platform, the mutual motion is much more complex and primarily defined by the dynamics of platform movement on the sea. For example, in the case of a speed boat, that has been used in the measurements described in Section V, the boat encounters and rides over the peaks of waves, resulting in a 'jumpy' motion. This causes randomly varying relative velocity during the integration time.

C. Range Migration and Doppler Smearing

Higher speed causes a wider Doppler spread from the scatterers and, therefore, a larger resolution refinement after DBS, while a higher CPI improves the signal to noise ratio (SNR) [41]. Both these factors enhance the imaging performance of the radar. However, if the Doppler shift changes across a MIMO frame repetition interval (MFRI), or range changes across the CPI, Doppler smearing and range migration, respectively, are expected to happen after range and Doppler compressions. This causes target defocusing along with a reduction in SNR.

The number of range bins traversed by a target during CPI, and the number of Doppler bins traversed by a target during MFRI are estimated as [42]:

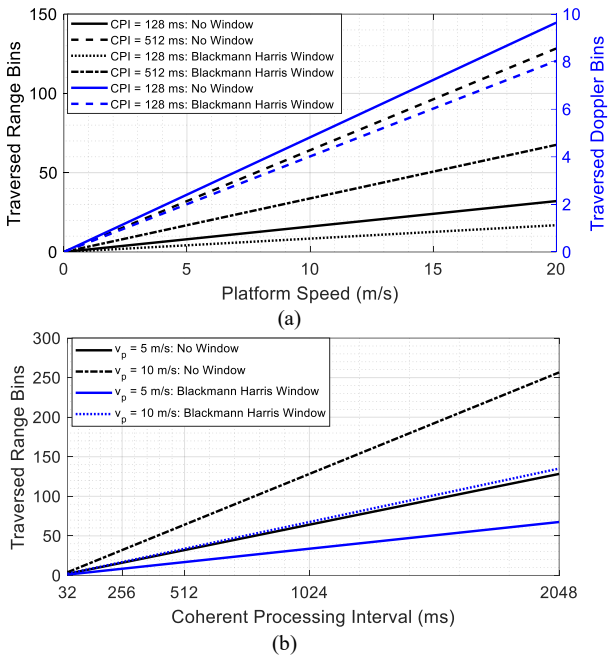

Fig. 8. Effect of platform speed (v_{p}) and coherent processing interval on range migration and Doppler smearing before and after spectral windowing with MFRI = 1 ms. (a) Range bins and Doppler bins traversed as a function of v_{p}. (b) Range bins traversed as a function of CPI for different platform speeds.

$$N_{\mathrm{R}} = \frac{v_{\mathrm{p}} CPI \cos\theta_{\mathrm{T}}}{\zeta_{\mathrm{RW}} \cdot \Delta R} \tag{24}$$

$$N_{\mathrm{Dop}} = \frac{f_{\mathrm{D}}}{\Delta f_{\mathrm{D}}} = \frac{2v_{\mathrm{p}} \cos\theta}{\lambda} \cdot \frac{MFRI}{\zeta_{\mathrm{DW}}} \tag{25}$$

where $\Delta R = c/2B$ is the range resolution for a bandwidth B, $\Delta f_{\mathrm{D}} = 1/MFRI$ is the Doppler resolution within a MIMO frame interval, ζ_{RW} and ζ_{DW} denotes the range and Doppler resolution degradations due to the applied spectral windows. Notably, in MIMO radars due to a larger equivalent chirp repetition interval, Doppler smearing increases compared to the traditional phased arrays.

SNR at a specific velocity v, denoted as SNR_{v}, is given as:

$$SNR_{\mathrm{V}} = \frac{SNR_{\mathrm{Static}}}{\sqrt{N_{\mathrm{Dop}} \cdot N_{\mathrm{Range}}}} \tag{26}$$

where SNR_{Static} is the SNR for a scene with stationary radar and target. Therefore, with increase in the range migration and Doppler smearing, SNR is expected to reduce.

The effects of platform speed and CPI on range migration and Doppler smearing are presented in Fig. 8 whereas their effect on SNR are presented in Fig. 9. The results are modelled for a MIMO radar with 4 transmit elements and 1 ms MFRI. The results do not consider additional range/ Doppler bins traversed due to wave motion, nor a potential vertical component of the platform velocity, which, if accounted would lead to a larger spread. SNR is estimated for a stationary point target of -10 dBsm RCS positioned at 20 m, 20° angle from the boresight of radar installed on a moving

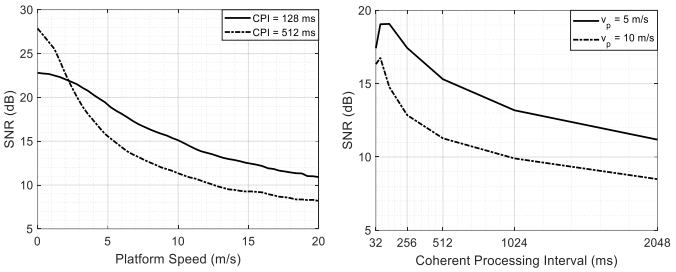

Fig. 9. SNR analysis. (a) Effect of platform speed (v_p) on SNR. (b) Effect of coherent processing interval on SNR.

platform. Radar configuration parameters are given in Table I. With the defined parameters, range resolution is 7.5 cm and cross-range resolution at 20 m from the radar is 7.3 cm. A Blackmann Harris window is used before range processing and Hann window is used before range-Doppler processing, giving $\zeta_{\mathrm{RW}} = 1.9$ and $\zeta_{\mathrm{DW}} = 1.2$ [43].

As expected, increase in both the platform speed and CPI makes the effect of range migration and Doppler smearing more critical with a significant reduction in SNR. The factor *MFRI* stays same with increase in CPI therefore, the number of traversed Doppler bins do not vary by changing CPI.

The processed radar images for three example cases are presented in Fig. 10. In the range-Doppler, different relative speeds are due to different aliasing factors, whereas FoV in the MIMO-DBS beamformed results is different due to a different platform speed as discussed in [44].

Range cuts corresponding to the range bin with maximum SNR for the cases discussed in Fig. 10 are shown in Fig. 11. The following key observations are made from Fig. 8 – Fig 11.

1) Doppler smearing, observed from the range-Doppler map, and range migration, observed from the beamformed plots, increase at higher speeds and CPI.
2) SNR reduces with an increase in the platform speed and CPI, which is a consequence of range migration and Doppler smearing.

The aforementioned factors limit the performance of MIMO-DBS beamformer as angular resolution improves with increase in both platform speed and CPI (shown in (15)).

As a trade-off to optimise both SNR and angular resolution after DBS processing, 128 ms CPI is used in the measurement results, after which SNR starts to decrease (shown in Fig. 9). Techniques such as in [45] have been investigated for range migration compensation. This, however, is beyond the scope of presented work.

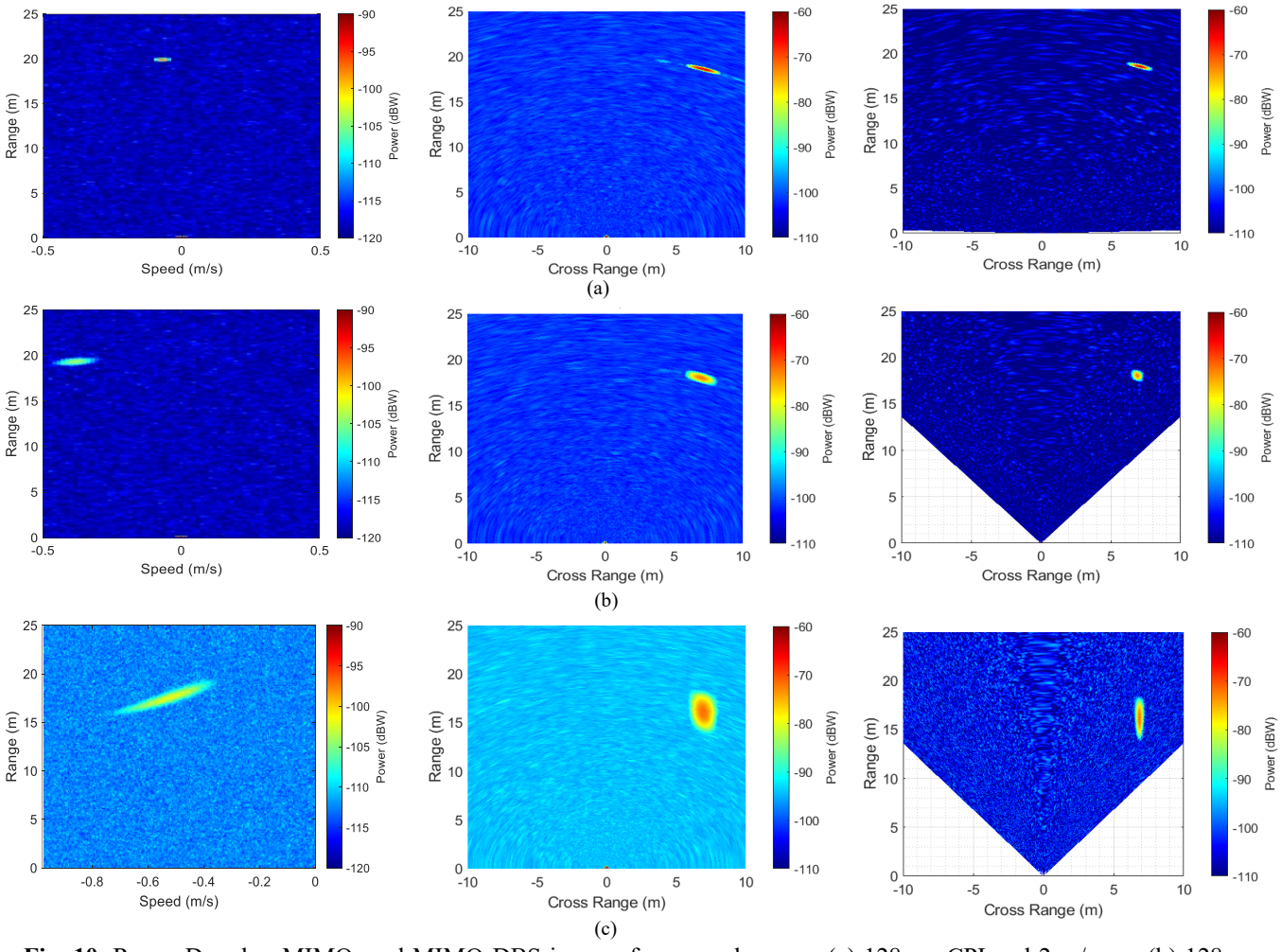

Fig. 10. Range Doppler, MIMO, and MIMO-DBS images for example cases. (a) 128 ms CPI and 2 m/s v_p. (b) 128 ms CPI and 10 m/s v_p. (c) 512 ms CPI and 10 m/s v_p.

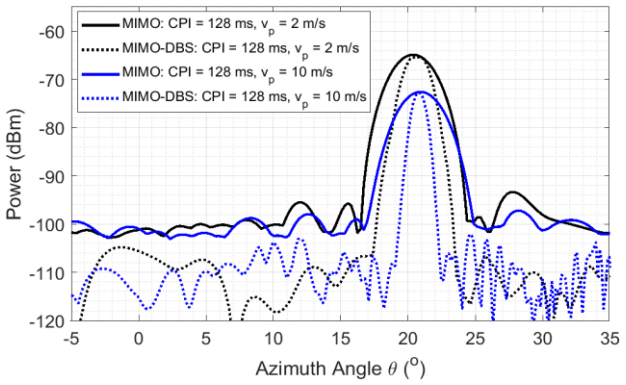

Fig. 11. MIMO and MIMO-DBS range cuts: (a) CPI = 128 ms, (b) CPI = 512 ms.

IV. Signal Processing

The block level representation of data processing chain used in this work is presented in Fig. 12. It is mainly divided into two steps. In the first step, high resolution imagery of stationary environment is generated using traditional MIMO-DBS algorithm discussed in Section II. In the second step, an adaptive MIMO-DBS approach is used to detect and focus multiple dynamic targets whilst achieving a high resolution.

Range and Doppler compressions on radar data along the fast-time and slow-time, respectively are applied to generate range-Doppler profile. This is followed by spatial compression on the data collected across array elements for MIMO beamforming. Using platform kinematics, DBS beamforming is applied after range-Doppler processing. The DBS and MIMO angles are then interpolated to the common grid for MIMO-DBS beamforming. To account for the Doppler frequency shift within a MIMO frame due to different transmission time of each transmit element (time division multiplexing (TDM) configuration), motion compensation as discussed in [27] is applied prior to MIMO and DBS beamforming. A symmetric four-term Blackmann Harris window is used before range processing and Hann window is used before Doppler processing and MIMO beamforming to reduce spectral leakage caused by FFT process.

To address the challenge of simultaneously detecting and focusing multiple 'dynamic' targets, we use a combination of adaptive thresholding for target detection, clustering, and adaptive MIMO-DBS (AMDBS) processing. This allows us to predict the relative velocity between the moving radar platform and dynamic targets to apply MIMO-DBS.

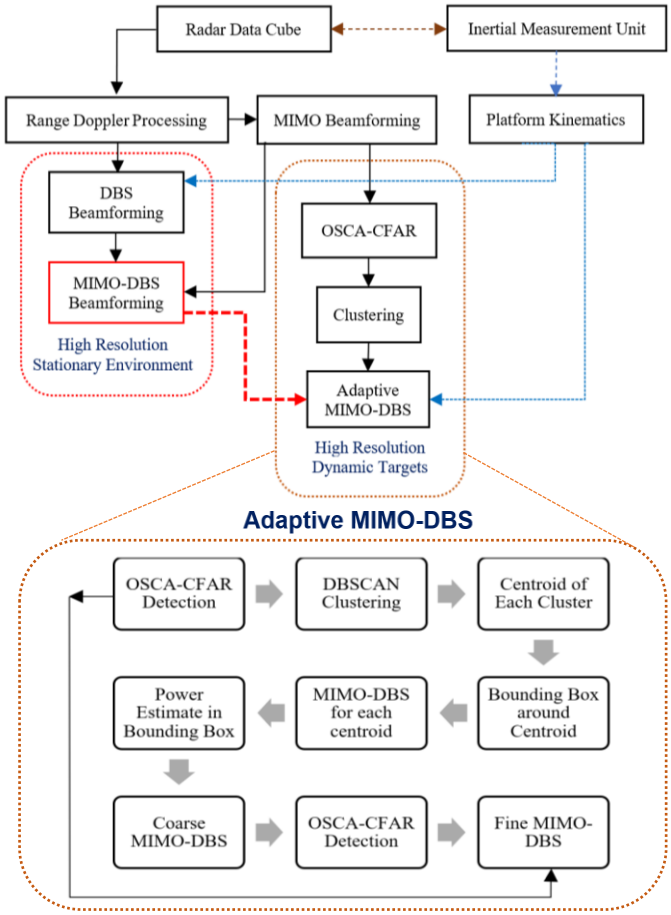

Fig. 12. Block level representation of data processing. OSCA-CFAR represents ordered statistic cell averaging – constant false alarm rate.

A. Target Detection

Firstly, we perform target detection from the MIMO beamformed imagery using ordered statistic cell averaging (OSCA) CFAR. In OSCA-CFAR, the detection threshold is adapted based on the order of power levels of cells in a reference window. This makes it robust to variations in the power levels and is particularly suitable in the case of multiple 'extended' targets with varying RCS values [46], [47].

For each azimuth bin, one-dimensional OS-CFAR is first applied to sort the range bins according to their magnitude, shown in (27), such that $X_{m,n} \le \cdots \le X_{k,n} \le \cdots \le X_{2,n} \le X_{1,n}$.

$$X_{\text{Sorted}}(m,n) = \begin{bmatrix} X_{1,1} & X_{1,2} & \cdots & X_{1,n} \\ X_{2,1} & X_{2,2} & \cdots & X_{2,n} \\ & \vdots & & \\ X_{k,1} & X_{k,2} & \cdots & X_{k,n} \\ & \vdots & & \\ X_{m,1} & X_{m,2} & \cdots & X_{m,n} \end{bmatrix} \tag{27}$$

where m and n represent the range and azimuth bins, respectively in the reference window. For a k-th order OS-CFAR, the k-th range bin is selected and CA-CFAR is applied along the azimuth dimension. The threshold, denoted as $T_{\text{OSCA-CFAR}}$, is estimated as:

$$T_{\text{OSCA-CFAR}} = \alpha \frac{1}{N_{\text{A}}} \sum_{i=1}^{N_{\text{A}}} X_{k,i} \tag{28}$$

where N_{A} represents the number of azimuth cells in CA-CFAR window and α is a scaling factor calculated as:

$$\alpha = \frac{-\ln\left(P_{\text{FA}}\right)}{\sum_{j=1}^{k} m-k+j} \tag{29}$$

where P_{FA} is the probability of false alarm.

It should be noted that the estimation presented in (29) assumes Gaussian statistics for the background clutter. Such statistics, though not representative for diverse range of sea clutter models, was however a good fit for our measured data recorded within the lake environment, where we observed a high signal to clutter plus noise ratio (SCNR). This is further elaborated in the subsequent sections. Nonetheless, at higher sea states, the clutter demonstrates non-Gaussian statistics. This, however, is outside the scope of presented work and will be investigated in our future work.

B. Clustering

In the next step, we cluster OSCA-CFAR detections to estimate the number and extent of targets. For this, we use Density Based Spatial Clustering of Applications with Noise (DBSCAN) [48] where clusters are generated based on the distance between detections. DBSCAN is particularly useful in maritime environment due to: 1) presence of arbitrary shaped targets such as buoys, swimmers, boats etc., and 2) appearance of potential outliers caused by the backscatter from sea surface and/or MIMO sidelobes.

The parameters required for DBSCAN are discussed next.

a) Search radius

All the detections within a search radius are assigned to the same target. To estimate this, we use an iterative algorithm based on the expected minimum and maximum number of detections per cluster. These are defined considering the dimensions of marine targets and the extent of clusters. For each value, DBSCAN is applied and the Euclidean distance between detections is used as a metric to assign detections to a cluster. The distances between all detections within a cluster are then sorted in an increasing order and the search radius for which number of required detections within a cluster increase significantly puts an upper limit on its value.

An example is demonstrated in Fig. 13 for expected number of detections per cluster (X) ranging from 3-7. Here, X = 6 will be used as an optimum value for the search radius.

With DBSCAN, described in Algorithm 1, the closely spaced targets with a different motion are assigned to different clusters. This is essential to focus them properly after AMDBS. An example would be a paddler with an oar, shown later in Fig. 18.

b) Performance evaluation of clustering

The Silhouette coefficient, denoted as S_{i}, is used as a metric to evaluate the clustering performance i.e., how well-separated the clusters are. S_{i} estimates the similarity of a detection to other detections in its own cluster, compared to those in other clusters, and is calculated as:

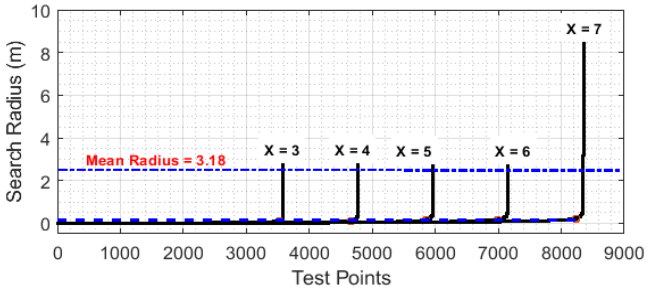

Fig. 13. Search radius for DBSCAN algorithm.

Algorithm 1 Description of DBSCAN

Initialising variables:
ClusterIdx = zeros(1,Number of detections); ClusterNo = 1;
R_s: search radius;
N_{min}: Minimum number of detections per cluster;
for I = 1:Number of Detections
a) Identify neighbourhood of each detection 'i'
Distance = Euclidean(Detection(i),Detections(:))
Neighbourhood = find(Distance <= R_s)
b) Identify outliers
if length(Neighbourhood) < N_{min}
IsOutlier(i) = true
c) Form cluster if detection not an outlier
ClusterIdx(i) = ClusterNo *%Assign point I to a cluster*
k = 1
while k <= length(Neighbourhood)
if IsOutlier(k)
Skip detection assignment as its outlier
k = k + 1
end
Repeat step(a) to update neighbourhood around each detection within the original neighbourhood
if ClusterIdx (k) == 0
ClusterIdx (k) = ClusterNo *%Assign detection to cluster if not already assigned*
end
end
ClusterNo = ClusterNo+1;

$$S_{\text{i}} = \frac{b_{\text{i}} - a_{\text{i}}}{\max\left(a_{\text{i}}, b_{\text{i}}\right)} \tag{30}$$

where a_{i} is the mean distance from i-th detection to other detections in its own cluster and b_{i} is the minimum mean distance from i-th detection to detections in a different cluster, minimised over the clusters. S_{i} value closer to 1 indicates good clustering performance i.e., well-separated clusters.

After generating clusters, the mean position of detections within each cluster gives the centroid of a cluster (target).

C. Adaptive DBS Methodology

To focus each target, we use an iterative algorithm where the velocity, v_{t}', is varied in the increments of velocity resolution and MIMO-DBS beamforming is applied for each value. The limits of v_{t}' are defined based wave speed due to sea state, denoted as v_{s}, margin according to the expected target motion, denoted as v_{RD}, and v_{p}. This gives:

$$v_{\text{p}} - v_{\text{s}} - v_{\text{RD}} \le v_{\text{t}}' \le v_{\text{p}} + v_{\text{s}} + v_{\text{RD}} \tag{31}$$

Within the integration duration of 128 ms (MIMO-DBS frame time) used in our work, we can assume near constant values of most of the parameters, for instance, the displacements and velocities, to give accurate enough estimates in (31).

For each value of v_t', mean power is estimated within the bounding box defined around the centroid of each cluster. The dimensions of bounding box are determined according to the extent of cluster. The value of v_t' for which mean power is maximum i.e., maximum SCNR is used to focus the target after AMDBS beamforming, calculated as:

$$v_t = \text{argmax}\left(v_t'\right)\left\{\frac{1}{N_{\text{bound}}}\sum_{i=1}^{N_{\text{bound}}} P\left(v_t'\right)\right\}_{t=1}^{T} \quad (32)$$

where T represents the total number of targets (clusters) and N_{bound} represents the number of resolution cells within the bounding box.

By changing the value of v_t', the corresponding DBS angle is also changed (see (11)) and SCNR is maximised when independent MIMO and DBS angles coincide after combined MIMO-DBS beamforming. This is illustrated in the modelled results in Fig. 14 for a stationary target positioned at 10 m, 50^o from the radar configured according to INRAS Radarlog. The platform velocity is 3 m/s. Point spread functions for MIMO and MIMO-DBS processes with different v_t' are shown in Fig. 14 (a) whereas range cuts at 10 m from the radar are shown in Fig. 14 (b) for each case. It can be seen that with a 0.3 m/s mismatch between the actual and assumed speeds, there is approximately 40 dB drop in the power which causes target defocusing after MIMO-DBS processing.

In the next step, MIMO-DBS maps generated after focusing each target are overlaid to obtain a coarse MIMO-DBS map. Due to overlaying, Doppler sidebands appear in the radar image which causes false targets. Sidebands are removed by performing OSCA-CFAR detection on the coarse MIMO-DBS map and the intersecting cells with the detection map obtained after applying OSCA-CFAR on MIMO beamformed imagery are retained to obtain a fine AMDBS map. It is to be noted that the performance of AMDBS might degrade if detections of targets with a different motion are not assigned to separate clusters. This will be discussed in Section VI.

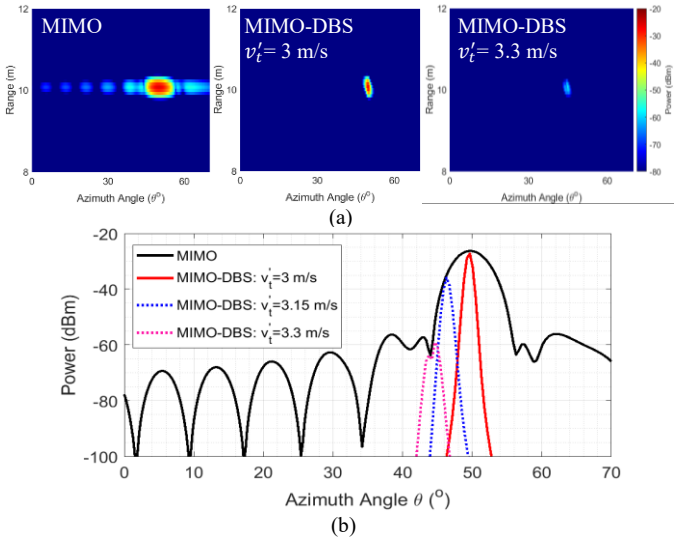

Fig. 14. Effect of v_t' of SNR. (a) Point spread functions for a point target after MIMO and MIMO-DBS beamforming; (b) Range cuts at 10 m for MIMO and MIMO-DBS beamformers.

Algorithm 2 Description of Adaptive MIMO-DBS (AMDBS) Algorithm.

(a) *Initialise variables and define velocity vector 'v_t''*
(b) *OSCA-CFAR on MIMO beamformed data followed by DBSCAN*
(c) *Estimate velocity to focus each target (maximise SNR)*
```
for i = 1:NumberTargets
  for j = 1:Number of Velocities
      DBSTune(j) = MIMODBSAlgorithm(MIMOdata,v(j))
      % Mean power within bounding box for i-th target
        P(j) = meanpower(DBSTune (Bounding box(i,j)))
        if max(P(j)): MIMODBSFocused(i) = DBSTune (j)
  end
end
```
(d) *Overlay focused MIMO-DBS maps*
(e) *OSCA-CFAR on coarse MIMO-DBS*
(f) *Intersecting regions of (b) and (e)*
```
Intersect = diff(DataStep(b), DataStep(e))
MinIdx  = min(Intersect) %minimum pixel indices
FineMIMODBS = MIMODBSOverlayed(MinIdx)
```

V. Measurements

To validate the presented approach, a measurement campaign was conducted at the Coniston Water in the UK. While the lake water can be quite rough in strong winds, during the measurements the weather was relatively calm. Based on wave heights, the lake condition can be estimated as equivalent to sea state 1 by the Douglas scale. Consequently, the clutter was rather low, giving a high SCNR. This allowed near 'laboratory' conditions to test the MIMO-DBS and AMDBS algorithms.

The sensing suite which was used to gather the data comprised a 77 GHz automotive FMCW-MIMO INRAS Radarlog operating in TDM MIMO mode with an equivalent virtual array of 61 elements, and a fibre optic gyro IMU [49] used to record platform kinematics [50]. The MIMO frame interval is 1 ms, where 4 chirps are sequentially transmitted, one from each transmit element of the radar. Each MIMO-DBS frame duration is 128 ms, composed of 512 chirps collected by the radar. In the DBS processing, 128 chirps have been used for Doppler processing for each Tx element of the radar, resulting in 0.015 m/s velocity resolution.

The sensing suite was installed on an inflatable motorboat in two different orientations: forward-looking from the nose of the motorboat, and backward-looking from the aft of the boat. The mean platform speed varied from 0.5 – 10 m/s during the measurements. The test scenario and the sensor suite setup are shown in Fig. 15 and the radar configuration parameters and expected performance are given in Table I. The radar and IMU were configured to record timestamped data for data fusion at the post-processing stage.

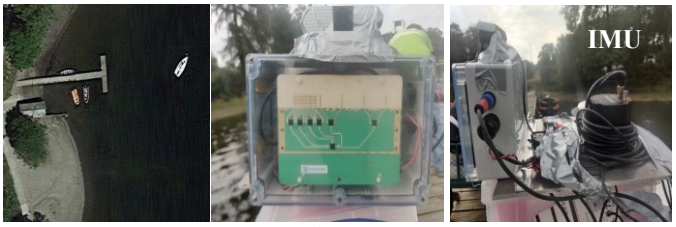

Fig. 15. Measurement setup, (a) aerial photo of the test scene, (b) automotive MIMO radar, (c) sensor suite.

VI. Results and Performance Analysis

The measured results in different scenarios are discussed in this section. The effects of range migration and Doppler smearing are negligible due to comparatively lower platform speed, lower sea state, and 128 ms CPI selected to have minimal range migration (Fig. 8). The raw sensing suite data corresponding to which measured results are shown is available at [51].

A. Single Target Scenario – Boat

In this scenario, an anchored 'quasi stationary' boat was imaged with the sensor suite installed in: a) backward-looking orientation with the platform moving away from it, and (b) forward-looking orientations with the platform moving towards it. Relative speed between the platform and the target is 3.1 m/s and 5.2 m/s for the two cases, respectively.

Fig. 16 and Fig. 17 shows the measured results for these cases, respectively. Output of MIMO beamformer is extracted from the Doppler cell containing the strongest signal.

Significant returns at closer ranges in Fig. 16 (b) and (c) corresponds to the strong wake at the back of the boat.

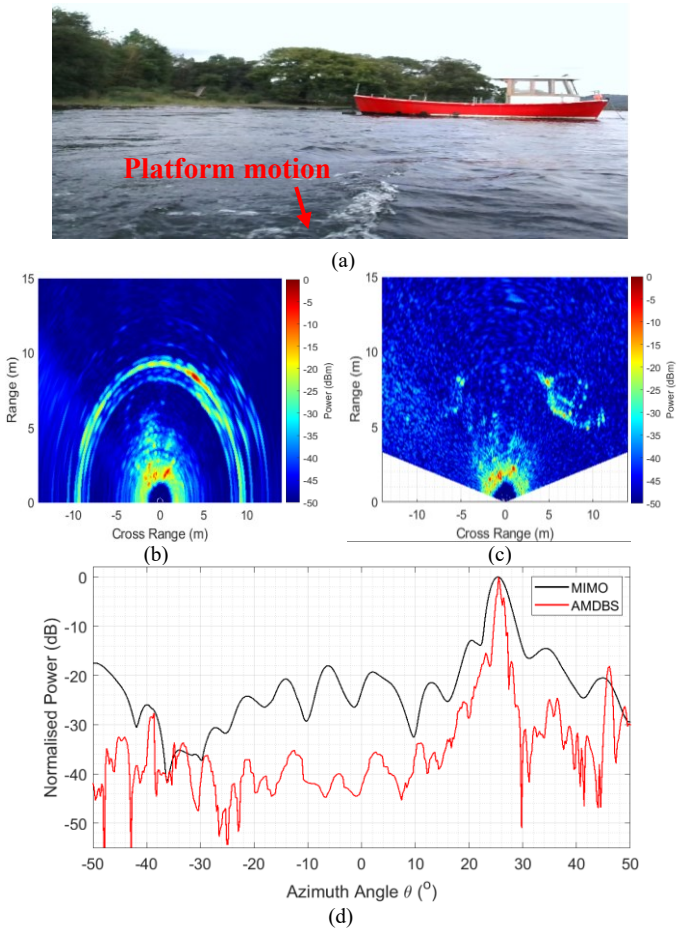

Fig. 16. Imagery of the boat with sensor suite installed in backward-looking orientation. (a) Image of the target, (b) output of MIMO beamformer, (c) output of AMDBS beamforming, (d) azimuth cross section of MIMO and AMDBS beamformers at 9.3 m range cut corresponding to the strongest reflector on the boat. The relative speed between platform and boat is 3.1 m/s.

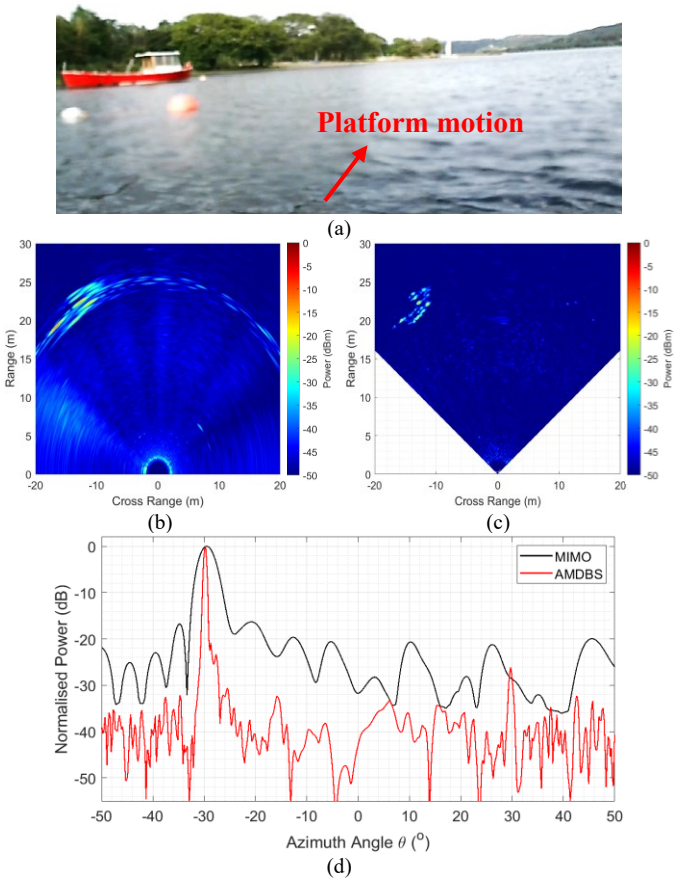

Fig. 17. Imagery of the boat with sensor suite installed in forward-looking orientation. (a) Image of the target, (b) output of MIMO beamformer, (c) output of AMDBS beamforming, (d) azimuth cross section of MIMO and AMDBS beamformers at 25.6 m range cut corresponding to the strongest reflector on the boat. The relative speed between platform and boat is 5.2 m/s.

In both the cases presented in Fig. 16 and Fig. 17, sidelobes after MIMO beamforming masks the scattering points on the boat thereby, reducing the dynamic range of radar. In contrast, AMDBS leads to significantly lower SLL, thus improving the SCNR, along with an improvement in the cross-range resolution to detect the scattering point of boat with high precision. This leads to a substantial improvement in the radar's ability to resolve the structure of boat.

Next, the SCNR and 3 dB resolutions of the two cases are estimated for the strongest reflector on the boat. In the first case, this corresponds to 9.3 m range cut (Fig. 16 (d)) with reflector at 25.4^{o}, whereas in the second case, this corresponds to 25.6 m range cut (Fig. 17 (d)) with reflector at 29.7^{o}. The results are presented in Table II. For each reflector, the background clutter to noise ratio (CNR) is estimated within a 5 m range and cross-range, centred on the reflector. Theoretical MIMO and AMDBS resolutions are estimated from (10) and (15), respectively.

As expected, with a larger speed, the resolution refinement factor also improves according to (16). The theoretical and measured resolutions in Table II have a close agreement for both the cases. The differences between resolutions can be

TABLE II
SCNR AND RESOLUTIONS OF MIMO AND AMDBS BEAMFORMERS.

	Case 1 $v_p = 3.1$m/s, $\theta_T = 25.4^o$	**Case 2** $v_p = 5.2$m/s, $\theta_T = 29.7^o$
	MIMO	
Theoretical	3.04^o	3.16^o
Measured	3.2^o	3.3^o
SCNR (dB)	24	31
	AMDBS	
Theoretical	0.9^o	0.49^o
Measured	0.82^o	0.54^o
SCNR (dB)	32	43
Resolution Refinement Factor		
	4	6
SCNR Improvement (dB)		
	7	11

accounted to multiple factors such as the accuracy of speed estimation and beam smearing due to array calibration factor applied to mitigate the effects of propagation path delay between multiple array elements [52]. As expected in the lake environment, the SCNR is also reasonably high.

B. Single Target Scenario - Paddler

In this scenario, two measurements were conducted with different relative positions of the paddler and the oar. The radar was installed in forward-looking orientation and the platform was moving towards the paddler.

1) In the first measurement (Case 1), the platform speed is 1.35 m/s and the strongest reflector on the oar is separated by 1.3 m from the paddler. The outputs of MIMO beamformer, OSCA-CFAR, and DBSCAN are shown in Fig. 18 (a), (b), and (c), respectively. For OSCA-CFAR, $P_{FA} = 10^{-6}$ and two-dimension reference window size is 20 x 25 bins across range and azimuth directions, respectively with a 15-th order OS-CFAR applied along the range axis.

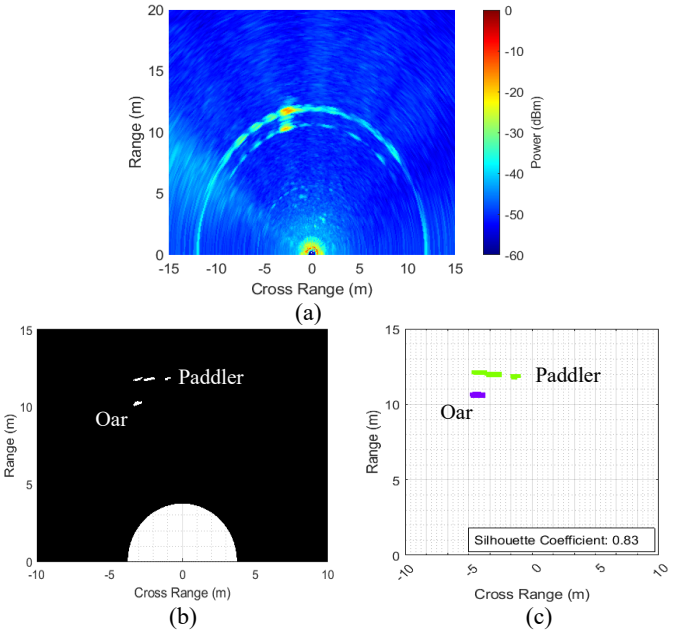

Fig. 18. Target detection and clustering on the paddler. (a) Output of MIMO beamformer, (b) output of OSCA-CFAR detector, (b) output of DBSCAN.

Due to both: different relative velocity and spatial separation of the paddler and the oar, they are assigned to different clusters with a mean Silhouette coefficient of 0.83. Each cluster is focused with a separate velocity v_t' in AMDBS process. The ground truth and beamformed results for this scenario are shown on the left side plots in Fig. 19.

2) In the second measurement (Case 2), the platform speed is 1.4 m/s and the oar and paddler are closer to each other. The corresponding ground truth and beamformed results are shown on right side plots in Fig. 19.

For both measurements, AMDBS focuses the scattering points of target having different relative speed w.r.t. the moving platform. Doppler sidebands that appear after traditional MIMO-DBS [53] are also suppressed.

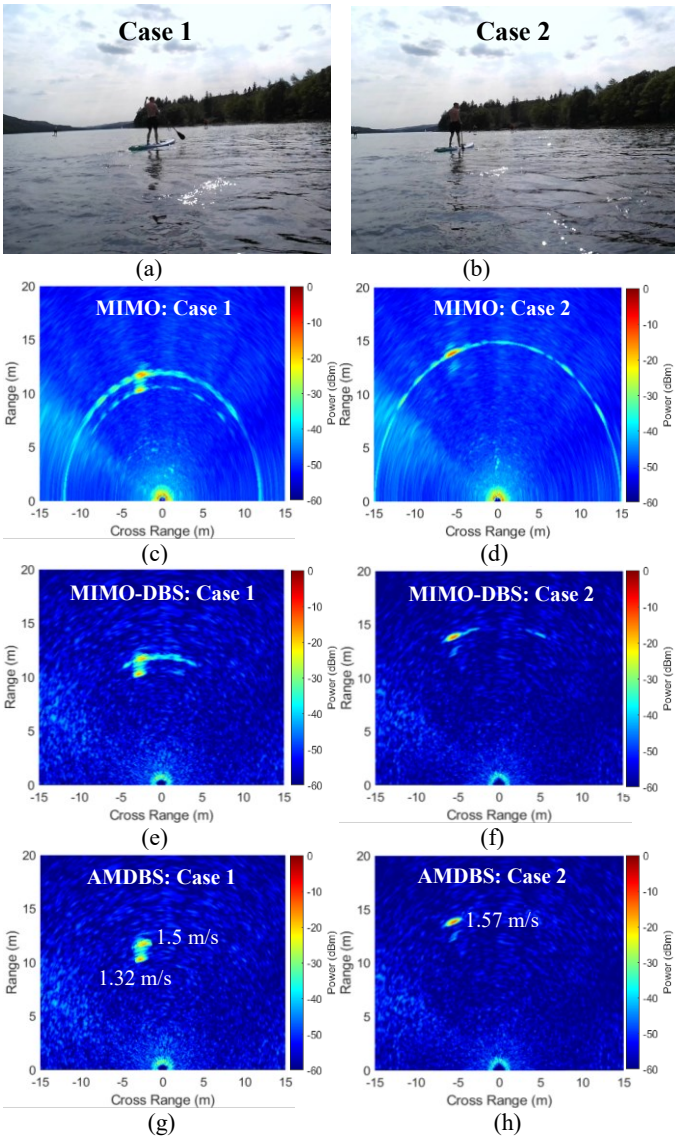

Fig. 19. Measured results of the paddler. (a) Ground truth: scene 1, (b) ground truth: scene 2, (c) MIMO beamforming: scene 1, (d) MIMO beamforming: scene 2, (e) AMDBS beamforming after step (c) in Algorithm 2: scene 1, (f) AMDBS beamforming after step (c) in Algorithm 2: scene 2, (g) output of AMDBS beamformer: scene 1, (h) output of AMDBS beamformer: scene 2.

Fig. 20. Ground truth for multi-target scenario presented as a series of camera frames.

SCNR improvement for the paddler in the discussed cases is approximately 15 dB after AMDBS beamforming. Due to relatively smaller platform speed and squint angle, resolution refinement factor is not significant, which is expected from the results presented in Fig. 3. Nevertheless, sidelobes are significantly reduced to enhance the radar's dynamic range.

C. Multi-Target Scenario

In the third scenario, a scene with multiple dynamic targets is imaged where each target has a different relative motion w.r.t. the moving platform. The ground truth images obtained from multiple consecutive camera frames (timestamped with radar) representing the whole scene are presented in Fig. 20 and the measured results are shown in Fig. 21. The radar is installed in backward-looking orientation with 1.63 m/s platform speed.

All the targets within radar FoV in Fig. 20 are focused using a separate velocity in AMDBS approach. The velocities used to focus each target in this case are: paddler 1: 2.1 m/s, paddler 2: 1.3 m/s, wake: 2.8 m/s, white boat: 1.63 m/s, motorboat: 1.62 m/s, and red boat: 1.54 m/s.

The SCNR of the imaged targets after the application of MIMO and AMDBS beamformers have been shown in Table III. For the scenario when a target is represented by multiple reflectors, its SCNR is estimated for the strongest reflector. It is worth noting, due to integration time required for DBS formation, some spikes expected from the sea surface, being uncorrelated, are expected to be averaged out. The impact of target's RCS on the observed SCNR is not addressed within the scope of this paper.

As discussed previously, sidelobes are suppressed along with the removal of Doppler sidebands (Fig. 21 (b)) resulting in a significant increase in the SCNR. As expected from (15), the targets off-boresight such as paddler 1, paddler 2, and the red boat have a larger resolution refinement compared to the targets closer to radar boresight (motorboat and white boat).

TABLE III
SCNR OF IMAGED TARGETS IN A MULTI-TARGET SCENARIO.

	MIMO (dB)	AMDBS (dB)	SCNR Improvement (dB)
Wake	13	27	14
White Boat	26	64	38
Motorboat	21	48	27
Red boat	33	53	20
Paddler 1	7	27	20
Paddler 2	8	28	20

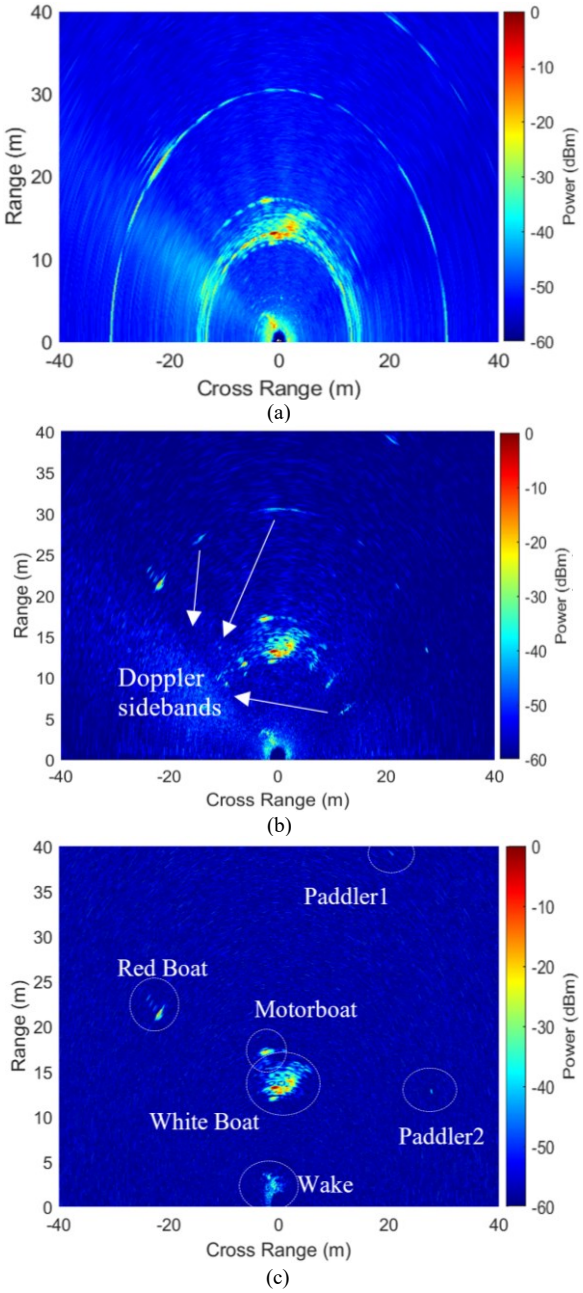

Fig. 21. Measurement results in the multi-target scenario. (a) Output of MIMO beamformer, (b) coarse MIMO-DBS map showing the appearance of Doppler sidebands. (c) Fine AMDBS map focusing each target.

D. Extended Target Imagery

With the provided resolution of MIMO sensor used for the measurements and with further refinement in the resolution using adaptive MIMO-DBS beamformer, nearly all the targets appear as extended, as discussed in the previous results. In this case, each target is represented by multiple scattering points. Additionally, by exploiting the potential sensitivity of mm-wave frequencies to the texture, we have imaged the full extent of maritime scene, which is demonstrated in Fig. 22.

The full extent of shore, a stationary background, is imaged, with a mean SCNR of 22 dB, using the platform speed obtained from IMU with is 2.5 m/s in this case. The boat is imaged using AMDBS algorithm with a relative speed of 2.62 m/s. The strongest reflector on the boat has a SCNR of 53 dB whereas the weakest imaged reflector has a SCNR of 23 dB. The high-resolution imagery of shore is suitable for the applications such as docking. Moreover, a superposition of stationary scene and dynamic targets allows a better understanding of the surroundings and provides useful information to target tracker and platform path planner.

VII. Computational Complexity

It is worth mentioning that to provide situational awareness to small and medium sized marine platforms, the practical sea states to take into considerations would be sea states 1 - 4. For these states, majority of the targets will either be floating with a small speed correlated with the speed of wave within the integration duration (order of ms) as in Fig. 7b or moving with a relatively small speed, such as swimmers, paddlers. In this scenario, the platform speed will be a dominant contributor to the relative speed between the platform and the moving targets. Nevertheless, as we use the bulk velocity as a reference to tune the relative velocity in (31), the required number of iterations (M) are significantly reduced.

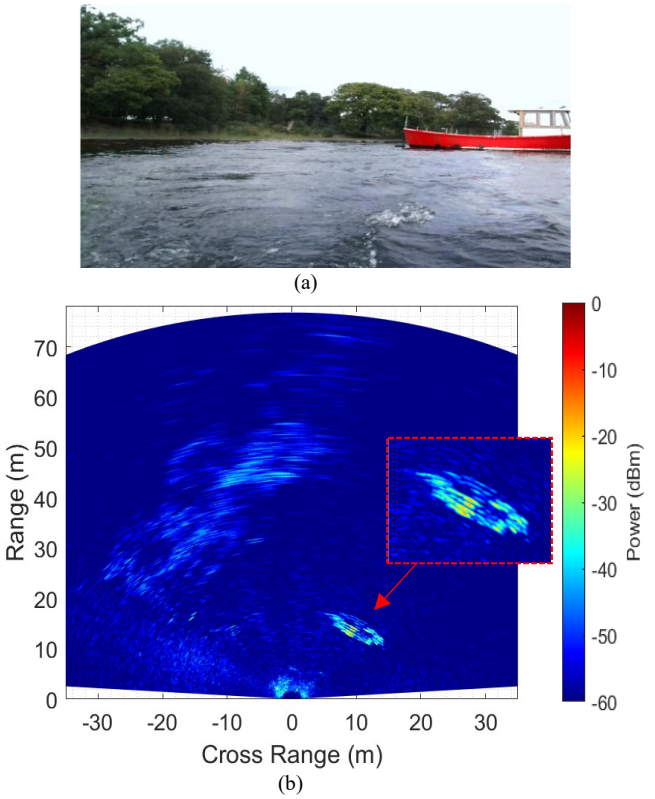

Fig. 22. Extended scene imagery: (a) ground truth, (b) output of AMDBS beamformer.

In terms of time consumption of DBS itself, we can potentially compare it with the time required to perform back projection in focussed synthetic aperture radar (SAR) case. One of the major advantages of DBS beamforming is that it is traditionally based on FFT with a computational complexity of $\underline{\mathrm{O}}\left(NP\log_2 NP\right)$ [54] for N-point FFT along fast-time and P-point FFT along slow-time, while for back-projection (BP) in SAR, the number of operations will be $\underline{\mathrm{O}}\left(NPN\right)$ [55], defining a significant processing time advantage for DBS.

In our work, with the same computer platform and MATLAB environment, the DBS processing takes a few ms while back-projection requires several minutes. With modern processors and the use of FPGAs, computational speeds can be further significantly increased with signal processing done at higher rates to enable real time imagery and even image segmentation [12] with statistical inference.

In the adaptive DBS process, for M required iterations to tune the velocity of N_T targets, the computational complexity can be expressed as $\underline{\mathrm{O}}\left(M\cdot N_T\cdot N\cdot P\log_2 NP\right)$. As $N_T \ll N, P$ the complexity of DBS is defined as: $\underline{\mathrm{O}}\left(MNP\log_2 NP\right)$ making the same processing time advantage with respect to BP if similar adaptive search of correct velocity is undertaken.

VIII. Conclusion

An approach to focus and enhance the resolution of multiple dynamic targets in a maritime environment is presented which combines traditional MIMO-DBS with adaptive detection, clustering, and adaptive focusing. It is shown that despite the dynamic nature of water surface, reasonable resolution refinement and SCNR improvement can be obtained through the application of DBS in a maritime environment using compact ‘automotive’ radar sensors. The finer resolution gives a potential for substantially superior target detection and classification and ultimately, reliable path planning.

The focus of this work is to provide superior imaging capability to the radar which will act as a pre-requisite for target classification. Target detection and clustering defines the "image of target" which can be used for classification of the class of object, but importantly it can be used as a two-class binary classification - normative (sea) vs anomalous (target). Classification itself is beyond the scope of this paper.

Future work will involve conducting measurements at higher sea states and higher platform speeds to test the performance of adaptive MIMO-DBS beamformer in more challenging environments. In these conditions, a varying SCNR is expected which will give rise to false alarms with clutter represented by non-Gaussian statistics. Such conditions will certainly affect target detectability but also importantly influence the mutual trajectories and dynamics of both

platform and the target. Currently we are developing simulation models to evaluate comprehensive mechanisms which can potentially affect imaging performance within the sea scene. We will also investigate phase alignment and entropy minimisation to improve target focusing. The effectiveness of OSCA-CFAR will be analysed and if needed, appropriate target detection techniques will be developed. Using high resolution imagery of marine targets obtained in various sea conditions, we will exploit the contrast between their returns in image segmentation and classification to generate results much closer to the camera imagery. Finally, target tracking and trajectory estimation will be developed for path planning applications.

ACKNOWLEDGMENT

This work is part of the project 'Sub-THz Radar sensing of the Environment for future Autonomous Marine platforms – STREAM,' which is being funded by EPSRC UK grant EP/S033238/1. The authors express gratitude to the staff of Raymond Priestley Sport Centre of the University of Birmingham for support to organise and conduct trials from their site and use their boats and jetty for trials. We also thank our colleagues from The University of Saint Andrews for useful discussions.

REFERENCES

[1] D. Gusland, B. Torvik, E. Finden, F. Gulbrandsen, and R. Smestad, 'Imaging radar for navigation and surveillance on an autonomous unmanned ground vehicle capable of detecting obstacles obscured by vegetation,' *IEEE Radar Conference (RadarConf)*, Apr.2019, pp. 1–6.

[2] G. Ludeno, A. Orlandi, C. Lugni, C. Brandini, F. Soldovieri, and F. Serafino, 'X-Band Marine Radar System for High-Speed Navigation Purposes: A Test Case on a Cruise Ship,' *IEEE Geoscience and Remote Sensing Letters*, vol. 11, no. 1, pp. 244–248, Jan. 2014.

[3] P. Shui, Z. Guo, and S. Shi, 'Feature-Compression-Based Detection of Sea-Surface Small Targets,' *IEEE Access*, vol.8, pp.8371–8385, 2020.

[4] P.-L. Shui, D.-C. Li, and S.-W. Xu, 'Tri-feature-based detection of floating small targets in sea clutter,' *IEEE Transactions on Aerospace and Electronic Systems*, vol. 50, no. 2, pp. 1416–1430, Apr. 2014.

[5] Z.-X. Guo, X.-H. Bai, P.-L. Shui, L. Wang, and J. Su, 'Fast Dual Trifeature-Based Detection of Small Targets in Sea Clutter by Using Median Normalized Doppler Amplitude Spectra,' *IEEE J. Sel. Top. Appl. Earth Observations Remote Sensing*, vol. 16, pp. 4050–4063, 2023.

[6] Z. Liang, J. Chen, and J. Jiang, 'A Multi-Featured Detection Method for Small Target on Sea Surface Based on GSP,' *IEEE Geoscience and Remote Sensing Letters*, vol. 20, pp. 1–5, 2023.

[7] J. Hu, W.-W. Tung, and J. Gao, 'Detection of low observable targets within sea clutter by structure function based multifractal analysis,' *IEEE Transactions on Antennas and Propagation*, vol. 54, no. 1, pp. 136–143, Jan. 2006.

[8] T. Gu, 'Detection of Small Floating Targets on the Sea Surface Based on Multi-Features and Principal Component Analysis,' *IEEE Geoscience and Remote Sensing Letters*, vol. 17, no. 5, pp. 809–813, May 2020.

[9] Y. Zhu, Y. Li, and Q. Zhang, 'False-Alarm-Controllable Radar Target Detection by Differentiable Neyman Pearson Criterion for Neural Network,' *IEEE Transactions on Geoscience and Remote Sensing*, vol. 61, pp. 1–14, 2023.

[10] S. Xu, H. Ru, D. Li, P. Shui, and J. Xue, 'Marine Radar Small Target Classification Based on Block-Whitened Time–Frequency Spectrogram and Pre-Trained CNN,' *IEEE Transactions on Geoscience and Remote Sensing*, vol. 61, pp. 1–11, 2023.

[11] C. Waldschmidt, J. Hasch, and W. Menzel, 'Automotive Radar — From First Efforts to Future Systems,' *IEEE Journal of Microwaves*, vol. 1, no. 1, pp. 135–148, winter 2021.

[12] Y. Xiao, L. Daniel, and M. Gashinova, 'Image Segmentation and Region Classification in Automotive High-Resolution Radar Imagery,' *IEEE Sensors Journal*, vol.21, no.5, pp.6698–6711, Mar.2021.

[13] A. A. Pirkani, S. Pooni, and M. Cherniakov, 'Implementation of MIMO Beamforming on an OTS FMCW Automotive Radar,' *20th International Radar Symposium (IRS)*, Jun. 2019, pp. 1–8.

[14] A. Danklmayer, G. Biegel, T. Brehm, S. Sieger, and J. Förster, 'Millimeter wave propagation above the sea surface during the Squirrel campaign,' *16th International Radar Symposium (IRS)*, Jun. 2015, pp. 300–304.

[15] M. D. Anguelova, 'Absorption and Scattering by Sea Foam Streaks at Millimeter-Wave Frequencies,' *IEEE International Geoscience and Remote Sensing Symposium*, Sep. 2020, pp. 5662–5665.

[16] S. Zainuddin, I. Pasya, N. E. A. Rashid, R. S. A. R. Abdullah, and A. R. Abdullah, 'Performance of MIMO FMCW Radar in Detecting Small Vessels,' *IEEE International RF and Microwave Conference (RFM)*, Dec. 2018, pp. 329–332.

[17] S. Zainuddin, N. E. A. Rashid, I. Pasya, and R. S. A. R. Abdullah, 'Simulation of Multi-band MIMO FMCW Radar Performance in Detecting Maritime Vessels,' *International Conference on Radar, Antenna, Microwave, Electronics, and Telecommunications (ICRAMET)*, Oct. 2019, pp. 113–117.

[18] G. Gennarelli, C. Noviello, G. Ludeno, G. Esposito, F. Soldovieri, and I. Catapano, '24 GHz FMCW MIMO Radar for Marine Target Localization: A Feasibility Study,' *IEEE Access*, vol. 10, pp. 68240–68256, 2022.

[19] Y.-S. Yoon, M. G. Amin, and F. Ahmad, 'MVDR Beamforming for Through-the-Wall Radar Imaging,' *IEEE Transactions on Aerospace and Electronic Systems*, vol. 47, no. 1, pp. 347–366, Jan. 2011.

[20] P. Stoica and A. Nehorai, 'MUSIC, maximum likelihood, and Cramer-Rao bound: further results and comparisons,' *IEEE Transactions on Acoustics, Speech, and Signal Processing*, vol. 38, no. 12, pp. 2140–2150, Dec. 1990.

[21] M. Hott, J. Mietzner, S. Lutz, M. Bockmair, and P. A. Hoeher, 'Joint Super-Resolution and Array Interpolation for MIMO Radar Virtual Arrays,' *15th European Radar Conference (EuRAD)*, Sep. 2018, pp. 126–129.

[22] S. Gishkori, D. Wright, L. Daniel, M. Gashinova, and B. Mulgrew, 'Imaging Moving Targets for a Forward-Scanning Automotive SAR,' *IEEE Transactions on Aerospace and Electronic Systems*, vol. 56, no. 2, pp. 1106–1119, Apr. 2020.

[23] N. Ustalli, G. Krieger, J. Mittermayer, M. Villano, and C. Waldschmidt, 'MirrorSAR Concept: Phase Synchronization Analysis,' *Kleinheubach Conference*, Sep. 2022, pp. 1–4.

[24] A. Laribi, M. Hahn, J. Dickmann, and C. Waldschmidt, 'Vertical digital beamforming versus vertical Doppler Beam Sharpening,' *IEEE 20th International Conference on Intelligent Transportation Systems (ITSC)*, Oct. 2017, pp. 1–6.

[25] A. Pirkani, S. Cassidy, F. Norouzian, M. Gashinova, and M. Cherniakov, 'Doppler Beam Sharpening for Enhanced MIMO Imagery in the Presence of Automotive Interference,' in *2021 18th European Radar Conference (EuRAD)*, Apr. 2022, pp. 417–420.

[26] L. Daniel *et al.*, 'Application of Doppler beam sharpening for azimuth refinement in prospective low-THz automotive radars,' *IET Radar, Sonar & Navigation*, vol. 12, no. 10, pp. 1121–1130, 2018.

[27] S. L. Cassidy, S. Pooni, M. Cherniakov, E. G. Hoare, and M. S. Gashinova, 'High-Resolution Automotive Imaging Using MIMO Radar and Doppler Beam Sharpening,' *IEEE Transactions on Aerospace and Electronic Systems*, vol. 59, no. 2, pp. 1495–1505, Apr. 2023.

[28] Z.-X. Guo, X.-H. Bai, J.-Y. Li, and P.-L. Shui, 'Fast Detection of Small Targets in High-Resolution Maritime Radars by Feature Normalization and Fusion,' *IEEE Journal of Oceanic Engineering*, vol. 47, no. 3, pp. 736–750, Jul. 2022.

[29] 'INRAS Products - RadarLog - RF-Frontends'. Accessed: Aug. 25, 2021. [Online]. Available: https://inras.at/en/radarlog/.

[30] A. Pirkani, D. Kumar, M. Cherniakov, and M. Gashinova, 'Distributed Automotive Radar Multi-Modal Sensing,' *20th European Radar Conference (EuRAD)*, Sep. 2023, pp. 319–322.

[31] J. A. Batlle and A. Barjau Condomines, *Rigid Body Dynamics*. Cambridge: Cambridge University Press, 2022.

[32] 'Longitudinal and Transverse Wave Motion'. Accessed: Jan. 10, 2023. [Online]. Available: https://www.acs.psu.edu/drussell/demos/waves/wavemotion.html

[33] T. Li, Z. Zhang, and D. Huang, 'Vibration analysis for marine radar frequency synthesis module,' *CAA Symposium on Fault Detection, Supervision, and Safety for Technical Processes (SAFEPROCESS)*, Dec. 2021, pp. 1–5.
[34] X. Liu, Z. Wu, T. Wu, Y. Li, and X. Li, 'The distinguish and statistical analysis of sea clutter spikes,' *3rd Asia-Pacific Conference on Antennas and Propagation*, Jul. 2014, pp. 1105–1108.
[35] 'Oceanography: waves'. Accessed: Jan. 27, 2023. [Online]. Available: http://www.seafriends.org.nz/oceano/waves.htm
[36] L. Y. Daniel, M. S. Gashinova, and M. Cherniakov, 'Target visibility estimation in a buoy mounted maritime forward scatter radar,' *IEEE Radar Conference (RadarCon)*, May 2015, pp. 0755–0760.
[37] M. Naderi and M. Pätzold, 'Design and analysis of a one-dimensional sea surface simulator using the sum-of-sinusoids principle,' in *OCEANS 2015 - MTS/IEEE Washington*, Oct. 2015, pp. 1–7.
[38] D. K. Barton, *Radar Equations for Modern Radar*. Artech House, 2013.
[39] K. Richter, P.-F. Wang, and J. M. Ayers, 'Measuring Seabed Pressure: a Search for Longuet-Higgins Events,' in *OCEANS 2021: San Diego – Porto*, Sep. 2021, pp. 1–6.
[40] S. A. Hsu, E. A. Meindl, and D. B. Gilhousen, 'Determining the Power-Law Wind-Profile Exponent under Near-Neutral Stability Conditions at Sea,' *Journal of Applied Meteorology and Climatology*, vol. 33, no. 6, pp. 757–765, Jun. 1994.
[41] A. Pirkani *et al.*, 'SINR Improvement Across the Automotive Radar Signal Processing Chain,' *19th European Radar Conference (EuRAD)*, Sep. 2022, pp. 5–8.
[42] A. Pirkani, D. Kumar, L. Daniel, E. Hoare, M. Cherniakov, and M. Gashinova, 'Dynamic Multi-Target Detection and Focus in Maritime Conditions,' *20th European Radar Conference (EuRAD)*, Sep. 2023, pp. 510–513.
[43] F. J. Harris, 'On the use of windows for harmonic analysis with the discrete Fourier transform,' *Proceedings of the IEEE*, vol. 66, no. 1, pp. 51–83, Jan. 1978.
[44] S. L. Cassidy, S. Pooni, E. G. Hoare, M. Cherniakov, and M. S. Gashinova, 'Analysis of MIMO-DBS performance for wide FOV automotive imaging,' in *International Conference on Radar Systems (RADAR 2022)*, Oct. 2022, pp. 237–242.
[45] A. Bourdoux and M. Bauduin, 'Near-optimal Range Migration and Doppler Ambiguity Compensation for FMCW Radars,' *IEEE Radar Conference (RadarConf22)*, Mar. 2022, pp. 1–6.
[46] B. Magaz, A. Belouchrani, and M. Hamadouche, 'Automatic Threshold Selection in OS-CFAR Radar Detection Using Information Theoretic Criteria,' PIER B, vol. 30, pp. 157–175, 2011.
[47] B. Yang and H. Zhang, 'A CFAR Algorithm Based on Monte Carlo Method for Millimeter-Wave Radar Road Traffic Target Detection,' *Remote Sensing*, vol. 14, no. 8, Art. no. 8, Jan. 2022.
[48] D. Deng, 'DBSCAN Clustering Algorithm Based on Density,' *7th International Forum on Electrical Engineering and Automation (IFEEA)*, Sep. 2020, pp. 949–953.
[49] 'Spatial FOG'. Accessed: Jan. 10, 2023. [Online]. Available: https://geo-matching.com/inertial-navigation-systems-ins/spatial-fog
[50] A. Pirkani *et al.*, 'Doppler Beam Sharpening for MIMO and Real Aperture Radars at mm-wave and Sub-THz Maritime Sensing,' *24th International Radar Symposium (IRS)*, May 2023, pp. 1–10.
[51] 'A. Pirkani and M. Gashinova, "STREAM - Sub-THz Radar sensing of the Environment for future Autonomous Marine platforms: RLG Dataset Coniston A". Zenodo, Nov. 06, 2023. doi: 10.5281/zenodo.10075384.'
[52] A. Pirkani, S. Cassidy, S. Pooni, M. Cherniakov, and M. Gashinova, 'Modelling and experimental validation of radar - environment interaction in automotive scenarios', in International Conference on Radar Systems (RADAR 2022), Oct. 2022, pp. 395–400
[53] S. L. Cassidy, S. Pooni, A. Pirkani, E. G. Hoare, M. Cherniakov, and M. S. Gashinova, 'Doppler Beam Sharpening for High-Resolution Imaging in Dynamic Automotive Scenes,' *19th European Radar Conference (EuRAD)*, Sep. 2022, pp. 325–328.
[54] L. Daniel and M. Gashinova, 'Sub-THz Radar Imagery for Automotive Application,' *19th European Radar Conference (EuRAD)*, Sep. 2022, pp. 261–264.
[55] H. Cruz, M. Véstias, J. Monteiro, H. Neto, and R. P. Duarte, 'A Review of Synthetic-Aperture Radar Image Formation Algorithms and Implementations: A Computational Perspective,' *Remote Sensing*, vol. 14, no. 5, Art. no. 5, Jan. 2022.

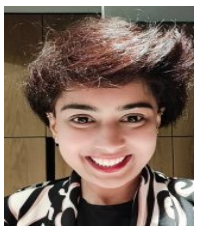

Anum Pirkani (Member, IEEE) received M.Sc. degree in RF and Microwaves from the University of Birmingham (UoB) in 2018, and the Ph.D. degree in Radar Systems from UoB in 2023. She has been involved with the Microwave Integrated Systems Laboratory (MISL) since 2017. She is currently working as a postdoctoral research fellow in MISL. Before joining MISL, she worked as a team lead RF and Microwave designing with 5 years' industrial experience. She has over 10 years combined academic and industrial experience in the design and development of radar systems. Her research interests includes radar signal processing, cognitive sensing, applications of radar systems for healthcare, and RF and microwave systems and devices. She has received the best paper award at EuRAD 2023 and best poster awards at EMSIG 2018 and 2022.

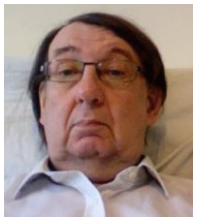

Andrew G. Stove (Senior Member, IEEE) received the B.A. degree in engineering science and the D.Phil. degree for work on surface acoustic wave devices from Oxford University, Oxford, U.K., in 1977 and 1981, respectively. In 1980, he joined Philips Research Laboratories in Redhill, U.K., where he worked on FMCW radar systems with applications in smart ammunition, automotive radar and low probability of intercept marine navigation. In 1996, he joined Racal Radar Defence Systems, which is now part of Thales, where he worked on the design for the Searchwater 2000 radar family, and on the analysis of the subsequent trials data, including improving the understanding of the behavior of the sea clutter. In 2015, he left Thales and he is currently working with the UoB, Birmingham, U.K. Dr. Stove is an Honorary Professor with the University of Birmingham and a Visiting Professor with UCL and is also a fellow of the Institution of Engineering and Technology (the successor of the Institution of Electrical Engineers).

Dillon Kumar received an MSci physics degree from the University of Birmingham, Birmingham, UK in 2019. He is currently studying for a PhD with the department of Electronic, Electrical and Systems Engineering at the University of Birmingham since 2019. His research interests include Sub-THz radar architecture, marine target detection, anomaly detection and Doppler beam sharpening and SAR. Mr. Kumar received the young engineer prize at the International Radar Symposium (IRS) 2023 for his work on DBS marine imagery using a 150 GHz radar system. He was one of the co-authors for the paper that won the best paper prize at the EuRad 2023 conference.

Mikhail Cherniakov graduated from Moscow Technical University in 1974. He received the Ph.D. degree in 1980 and the D.Sc. degree in 1992. He was a Full Professor in 1993. In 1994, he was a Visiting Professor with the University of Cambridge. In 1995, he moved to the University of Queensland, Australia. In 2000, he joined the School of EESE, Birmingham. Here, he founded the Microwave Integrated Systems Laboratory. He is the Chair of the Aerospace and Electronic Systems, University of Birmingham, U.K, with more than 40 years' experience on the R&D in radar systems. His research interests are in forward scatter and multistatic radar, active and passive radar, automotive, and short range sensors. He is the author/editor/coauthor of five books. He has more than 250 peer-reviewed publications. In 2017, he received the Christian Hulsmeyer Award for his achievements in radar research and education.

Marina S. Gashinova received the M.Sc. degree in math from Saint Petersburg State University in 1991, and the Ph.D. degree in physics and math from Saint Petersburg Electrotechnical University, Russia, in 2003. In 2006, she joined the Microwave Integrated System Laboratory (MISL), University of Birmingham (UoB), where she is the Chair of Pervasive Sensing. She is also the Head of the Pervasive Sensing Group, MISL, leading a number of research projects on automotive sensing and THz sensing. Her area of interests include active and passive radar, imaging THz sensing for ground and spaceborne scene assessments, cognitive radar, and deep neural networks classification.